Master's of Science Thesis

Commissioning of a Paul trap for Collinear Laser Spectroscopy of Exotic Radionuclides performed in a 30 keV MR-ToF device

Louis Croquette

Department of Physics

McGill University, Montreal

March 2023

A thesis submitted to McGill University in partial fulfillment of the requirements of the degree of a Master's in Science.

Contents

Abstract

The Multi-Ion Reflection Apparatus for Collinear Laser Spectroscopy (MIRACLS) is a novel experiment with the goal of performing high-resolution collinear laser spectroscopy (CLS) in a multiple-reflection time-of-flight (MR-ToF) device. By trapping ions and revolving them around a few thousand times in an optical detection region (ODR), significant gains in experimental sensitivity can be achieved compared to a single passage in conventional CLS. This increase will allow for studying exotic radionuclides that are produced with low yields, thus opening a new region of the nuclear chart to CLS experiments.

In order to fully benefit from the MIRACLS approach, the MR-ToF device requires cooled ion bunches with strict emittance requirements. This necessitates the use of a dedicated Paul trap tailored to match ion-bunch properties to the MR-ToF instrument requirements.

In this thesis, a description of the goals of MIRACLS and its experimental setup is provided, as well as the requirements for optimal MR-ToF and CLS performance. The experimental setup for commissioning and characterization of this new Paul trap is described in detail. The experimentally obtained temporal bunch width is compared with the demands of the MR-ToF instrument. The Paul trap is shown to be able to provide ion bunches with temporal widths of 123 ns, well matched to perform highly sensitive CLS in the MIRACLS MR-ToF device.

Résumé

L'appareil à temps-de-vols multi-réflecteur pour spectroscopie au laser colinéaire (MIRACLS) est une nouvelle expérience avec l'objectif de réaliser des études de spectroscopie au laser colinéaire (CLS) dans un appareil à temps-de-vols multi-réflecteur (MR-ToF). En piégeant des ions et les faisant recirculer plusieurs milliers de fois dans une région de détection optique (ODR), des augmentations importantes dans la sensibilité expérimentale par rapport à un passage unique dans des études CLS conventionnels peuvent être atteintes. Ces augmentations permettront l'étude d'isotopes radioactifs exotiques produits avec de faibles rendements et rendront plus accessibles des nouvelles régions de la carte nucléaire.

Pour réaliser les bénéfices de cette expérience au complet, l'appareil MR-ToF nécessite des ensembles refroidis d'ions avec des exigences strictes d'émittance. Ceci oblige l'utilisation d'un piège Paul dédié à la capture et refroidissement d'ions, afin de créer des ensembles qui satisfassent les besoins de l'instrument MR-ToF.

Dans cette thèse, une description des objectifs de MIRACLS et de son installation expérimentale est fournie, ainsi que les exigences pour l'opération MR-ToF et CLS optimale. L'installation expérimentale pour la mise en service et caractérisation du piège Paul est détaillée. La longueur temporelle d'un ensemble déterminée expérimentalement est ensuite comparée aux exigences de l'instrument MR-ToF. Le piège Paul a démontré la capacité à fournir des ensemble d'ions avec des longueurs temporelles de 123 ns, ce qui est supérieur aux exigences pour accomplir des études de CLS à haute sensibilité dans l'appareil MR-ToF de MIRACLS.

Acknowledgements

When I first committed to a Master's degree in January 2020, the initial plan for the research component was vastly different (global pandemics are difficult to anticipate!). Nevertheless, I am grateful that I chose to pursue this opportunity. Numerous challenges came up during this degree, and I have many people to thank for their continued support during my time at MIRACLS.

I would like to thank my research supervisor Stephan Malbrunot-Ettenauer for giving me the opportunity to do research at CERN, which was a dream come true. I appreciate the valuable physics discussions we had, his leadership of the MIRACLS collaboration, and his editorial support for this thesis.

A huge thanks to my academic supervisor Fritz Buchinger for always being willing to provide help wherever needed, including any administration related to my work. I also value the insights he shared during the conversations we had and the editing of this thesis.

The MIRACLS team made the work environment motivating and the enjoyable. Thank you to Markus Vilen for teaching me an incredible amount about developing a technical system, and for leading the design and development of the 30 keV MIRACLS MR-ToF system. I would also like to thank Markus, Simon Lechner, Fabian Hummer, and Anthony Roitman, for their enthusiastic and collaborative spirits, and for their strong support in data taking and data analysis. It was a great experience to work with these colleagues and Peter Plattner to build, test, and commission this ion trap system. I will look back fondly at the time we spent together at ISOLDE, whether it was working long nights, discussing active system schemes, or enjoying a cup of hot coffee.

Thanks to Simon, Carina Kanitz, Markus, and Franziska Maier for laying the groundwork and support with their simulations and design work of the Paul trap, and being readily available to answer anytime I had questions.

Furthermore, I would like to thank all team members of the MIRACLS collaboration, especially Erich Leistenschneider, Russell Blakey, Miranda Nichols, Ivana Belosevic, Rane Simpson, Frank Weinholtz, Paul Fischer, Wilfried Nortershauser, Eleni Ganze, Mia Au, Varvara Lagaki, and Lara Bartels.

Lastly, I would like to thank my family and friends for their unwavering support and encouragement; my parents Marc and Anne, my siblings Charlotte and Pierre, and my partner Mei.

List of Figures

List of Tables

Acronyms

CLS Collinear Laser Spectroscopy.

DAQ Data AcQuisition.

EPICS Experimental Physics and Industrial Control System.

FWHM Full-Width Half-Maximum.

GPS General Purpose Separator.

HRS High-Resolution Separator.

HV High-voltage.

ISOL Isotope Separation OnLine.

ISOLDE Isotope Separator OnLine DEvice.

MIRACLS Multi-Ion Reflection Apparatus for Collinear Laser Spectroscopy.

MR-ToF Multiple-reflection time-of-flight.

ODR Optical Detection Region.

PMT Photo-Multiplier Tube.

PSU Power Supply Unit.

PUMA antiProton Unstable Matter Annihilation.

RFQ RadioFrequency Quadrupole.

RIB Radioactive Ion Beam.

SLAC Stanford Linear Accelerator Center.

ToF Time of Flight.

1 Introduction

The development of ion traps in the 1950's and 1960's significantly accelerated new physics discoveries and advances. Wolfgang Paul's proposal for a "New mass spectrometer without a magnetic field" in 1953 paved the way for the development of a radiofrequency quadrupole trap, now known as a Paul trap [1]. Meanwhile, Hans Dehmelt developed a device that was able to trap an electron using a combination of electric and magnetic fields; he named this apparatus a "Penning trap", after Frans Penning who had done much of the early research into electron confinement via a magnetic field (in order to increase the sensitivity of a vacuum gauge). Since then, multiple areas of physics have seen significant progress such as precision measurements of the electron's magnet moment [2–4], determining the electron/proton mass ratio [5], or demonstrating charged particle/anti-particle (CPT) symmetry using electron-positron magnetic moments and mass ratios [6]. In 1989, Wolfgang Paul and Hans Dehmelt won the Nobel prize in physics for their efforts in developing ion traps [7].

Paul traps continue to be of major importance in many fields of physics. In the realm of nuclear physics, for instance, these devices are routinely employed as cooler-bunchers to prepare cooled and bunched beams for a variety of experimental techniques including the measurement of atomic masses and charge radii of short-lived radionuclides.

One such technique is collinear laser spectroscopy (CLS), where a narrow-band continuous wave laser is overlapped with a bunched ion beam to resonantly excite atoms and probe their hyperfine structure. Observing the fluorescence yield as a function of laser frequency reveals the hyperfine spectrum from which conclusions about nuclear ground state properties can be drawn. In modern CLS applications at radioactive ion beam (RIB) facilities, Paul traps are needed to accumulate these exotic ions before they are released in a short ion bunch with a temporal width of $\sim 1\,\mu s$. This allows experimentalists to gate their analysis on the ion-bunch passage through the laser-ion interaction and optical detection region and consequently improve the signal to background ratio by many orders of magnitude.

Radionuclides, far from the valley of stability but accessible at low energy branches of RIB facilities, typically exhibit short lifetimes on the order of a few milliseconds. In order to study these rare isotopes, the on-demand production and delivery of these radioactive

atoms is necessary. The new Multi-Ion Reflection Apparatus for Collinear Laser Spectroscopy (MIRACLS) is being developed and constructed at ISOLDE, CERN's facility for the production and delivery of these short-lived elements. The experiment will use a novel technique of performing CLS inside a Multiple-Reflection Time-of-Flight (MR-ToF) ion trap. This device is able to significantly extend the observation time of a measurement and thus improve the experimental sensitivity by up to a factor of a few hundred compared to conventional CLS.

The CLS technique and MR-ToF instrument both have stringent requirements for successful measurements and operation. In order to meet these demands, a dedicated Paul trap has been built to prepare the ion bunch prior to its injection into the MIRACLS MR-ToF device, where the highly sensitive CLS measurement takes place. This Paul trap must be able to trap a 60 keV continuous ion beam from ISOLDE, to efficiently accumulate and bunch the ions, as well as release the ions in a well-defined ion bunch. This will reduce the bunch's energy spread and temporal width such that the ions can be used for CLS in the MIRACLS MR-ToF device.

In this thesis, the installation and commissioning of the new Paul trap at MIRACLS' high resolution apparatus will be described, which represents the main contribution of the author to the project. Chapter 2 will discuss the necessary theoretical background to understand the motivation behind MIRACLS, covering the nuclear and atomic shell models, as well as atomic fine and hyperfine structures. Chapter 3 will continue with a description of the MIRACLS principle and how MR-ToF devices and Paul traps can be utilized to improve CLS measurements. Chapter 4 will cover the experimental setup for commissioning and testing the Paul trap. Chapter 5 will introduce and discuss the results of the experimental characterization of the Paul trap. Chapter 6 will conclude this thesis.

2 Background

Laser spectroscopy is a powerful experimental method to reveal important information about the structure of atomic nuclei. This section will outline the theoretical background necessary to understand how results from collinear laser spectroscopy, and therefore the MIRACLS experiment, can be used to validate and challenge theoretical models that describe atomic nuclei.

2.1 Nuclear theory background

2.1.1 Nuclear Shell Model

The nuclear shell model was first proposed in 1932 by D. Ivanenko and E. Gapon and further developed by M. Goeppert Mayer and J. H. D. Jensen in 1949, for which work they earned the 1963 Nobel prize [8]. To this day, the model is successful in explaining many observed nuclear phenomena, and continues to form the basis for many modern theoretical approaches. The nuclear shell model attempts to explain the internal arrangement of nucleons inside the atomic nucleus and its effects on numerous nuclear properties, such as nuclear charge radius, binding energies, excitation energies, etc. In particular, the behavior of the atomic nucleus as a function of number of nucleons is of interest. As an example, Figure 1 shows the (a) single-, S_N, and (b) double-neutron separation energy, S_{2N}, for calcium isotopes as a function of neutron number. Two interesting phenomena can be observed. First, there is the see-saw structure in the single-neutron separation energy S_N, which is explained by nucleons strongly coupling together, forming a pair [9]. When removing one neutron (or analogously one proton) from a nucleus with an even number of neutrons (or protons), it is necessary to first break the pair, which requires more energy [10]. In order to isolate the nuclear pairing effect from other changes in the nuclear structure, one often looks at the two-neutron separation energy S_{2N}.

The second phenomena observed is a sharp discontinuity at $A = 40$ (and also at $A = 48$). This is a feature explained by the nuclear shell model, in which specific nucleon numbers lead to a closed nuclear shell. These magic numbers are $N = 2$, 8, 20, 28, 50, 82, and 126 [11].

Considering that a calcium atom contains 20 protons, the drop in S_{2N} reflects the neutron shell closures at $N = 20$ and $N = 28$. In the traditional shell model, the shells for protons and neutrons are fully independent of each loading, leading to doubly-magic nuclei such as ^{48}Ca and ^{208}Pb in which both neutrons and protons entirely fill their respective shells.

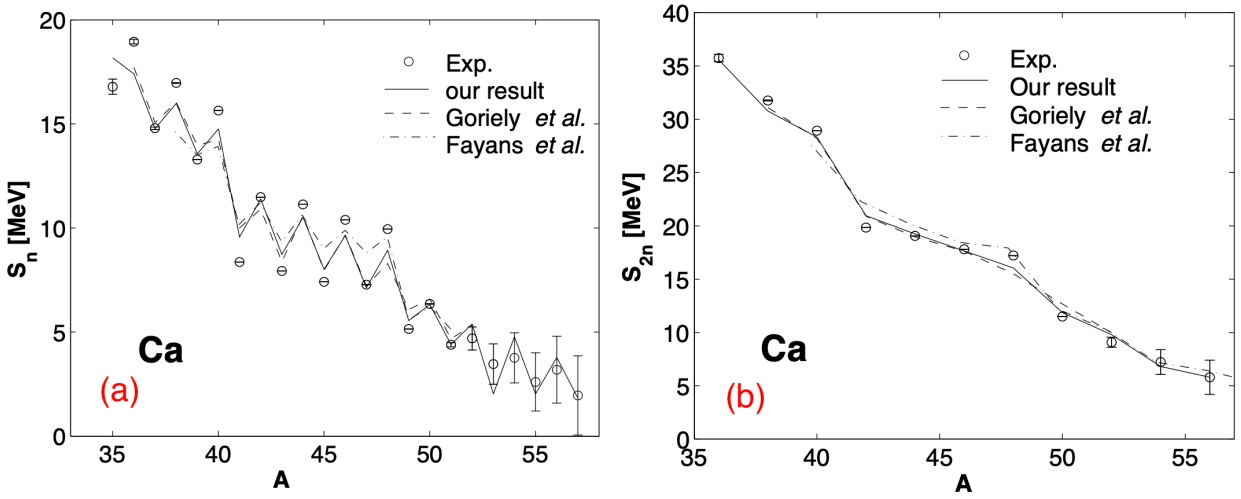

Figure 1 – (a) One neutron separation energy S_N as a function of atomic mass. (b) Two neutron separation energy S_{2N} as a function of atomic mass. Adapted from [12].

In addition to the separation energy, nuclear shell closures also affect many other observables. These include nuclear charge radii, with significant differences in mean square radii apparent near magic numbers. Figure 2 shows (a) the differences in mean-square charge radius, $\delta\langle r^2\rangle$, and (b) absolute charge radii, R_{ch}, as a function of the number of neutrons for potassium (K) isotopes. As the number of neutrons increases, so does the charge radius of the nucleus. The stabilizing effects of the $N = 28$ shell closure clearly manifests in these plots as a relative reduction in the charge radii.

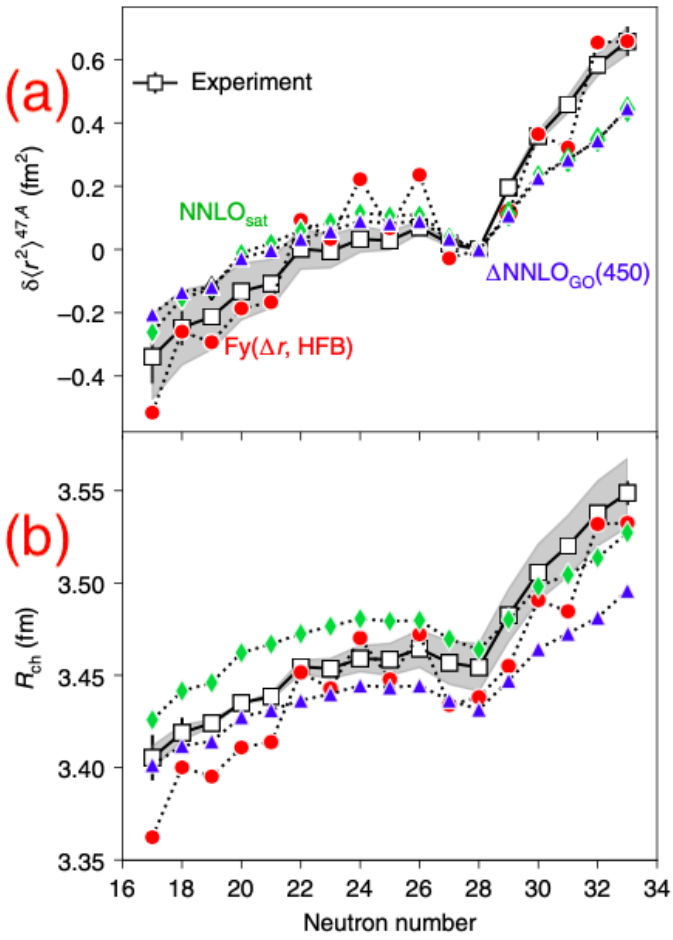

Figure 2 – (a) Differences in mean-square charge radii relative to ^{47}K ($Z = 19$) (b) Absolute charge radii. From [13].

2.1.2 Nuclear ground state properties

In order to validate and refine modern nuclear models, it is necessary to study properties of a nucleus, especially of short-lived radionuclides far away from stability. The primary tool for probing nuclei at MIRACLS is collinear laser spectroscopy (CLS), where a narrow-band continuous wave laser is used to resonantly excite ions to a higher energy state and then observe fluorescence photons. When counting the number of observed photons as a function of laser frequency, atomic hyperfine spectra are recorded which allow experimentalists to deduce characteristics of the atomic nucleus such as the nuclear spin, the nuclear magnetic dipole moment, the nuclear electric quadrupole moment, and the nuclear charge radius. Hence, via the hyperfine interaction between the atomic nucleus and its surrounding electron

cloud, nuclear properties are imprinted into the atomic spectrum.

Nuclear spin Nuclear spin is the total angular momentum of an atomic nucleus, and is defined by:

$$I = \sum_n j_n = \sum_n (l_n + s_n) \tag{1}$$

where l is the orbital angular momentum, s is the intrinsic angular momentum, and j is the total angular momentum of a nucleon n, which has to be summed over all nucleons in order to obtain the total spin I for the nucleus. Nuclear spin is dependent on the number of each type of nucleon, and can either be integer or half-integer. Due to the nuclear pairing effect, a pair of like-nucleons couples to a combined angular momentum of 0. Thus, the ground state of an even-even nucleus has a spin of 0. Even-odd nuclei have half-integer spin, and odd-odd nuclei have integer spin.

Nuclear magnetic dipole moment The nuclear magnetic moment arises from the spin and orbital angular momentum of the protons and neutrons in the atomic nucleus. The nuclear magnetic dipole moment is given by:

$$\hat{\mu} = g\hat{I}\mu_N = g\hat{I}\frac{e\hbar}{2m_p} \tag{2}$$

where g is the nuclear g-factor, $\hat{I}$ is the spin of the nucleus as defined above, μ_N is the nuclear magneton, e is the elementary charge, $\hbar$ is the reduced Planck constant, and m_p is the rest mass of a proton. Since it is dependent on the nuclear spin, ground states of even-even nuclei will not have a magnetic dipole moment, though even-odd and odd-odd nuclei will exhibit magnetic dipole moments. Since all paired nucleons couple to zero spin, only the unpaired nucleons are expected to contribute to the dipole moment. In the case of only one unpaired nucleon, the magnetic moment is thus assumed to be entirely due to this nucleon's combined spin and orbital angular momenta. For total moment μ, this has the form:

$$\mu = jg_j = \frac{j(j+1) + l(l+1) - s(s+1)}{2(j+1)}g_l + \frac{j(j+1) - l(l+1) + s(s+1)}{2(j+1)}g_s \tag{3}$$

where g_l and g_s are the Landé g-factors for orbital and spin angular momentum, respectively. For a free proton $g_l = 1$ and $g_s \approx 5.6$, and for a free neutron $g_l = 0$ and $g_s \approx -3.8$. Since $j = l \pm \frac{1}{2}$, Equation 3 simplifies to $\mu = g_l(j - \frac{1}{2}) + g_s\frac{1}{2}$ for $j = l + \frac{1}{2}$, and $\mu = g_l\frac{j(j+\frac{3}{2})}{j+1} - g_s\frac{j}{2(j+1)}$ for $j = l - \frac{1}{2}$ [14]. Section 2.3 will cover how the nuclear magnetic dipole moment interacts with the magnetic field generated by electrons surrounding the atomic nucleus, and, together with the nuclear electric quadrupole moment, cause the hyperfine splitting of energy levels.

Nuclear electric quadrupole moment The nuclear electric quadrupole moment, Q, describes the shape of the nuclear charge distribution. A Q value of 0 indicates a perfectly spherical charge distribution, while $Q > 0$ indicates an American-football shape distribution and $Q < 0$ indicates a cushion-like shape distribution, as shown in Figure 3. For a given angular momentum state I the electric quadrupole moment is defined by:

$$Q = \langle IM = I|\hat{Q}_0|IM = I\rangle \tag{4}$$

where $\hat{Q}_0 = \sum_i e_i(2z_i^2 - x_i^2 - y_i^2)$. It is experimentally known that electric quadrupole moments of even-even nuclei with $I = 0$ will also have a quadrupole moment of zero [15].

The quadrupole moment discussed above is considered to be the experimentally observed quadrupole moment. However, it is also possible to construct an intrinsic quadrupole moment Q' relative to the symmetry axis of a non-spherical nucleus [16]. This can be related to the observable moment by:

$$Q = \frac{I(2I-1)}{(I+1)(2I+3)}Q' \tag{5}$$

Clearly for $I = 0$ and $I = \frac{1}{2}$, $Q = 0$, despite Q' not necessarily being zero. This can be interpreted as a nucleus with zero spin is unable to be characterized as having a preferred direction in space.

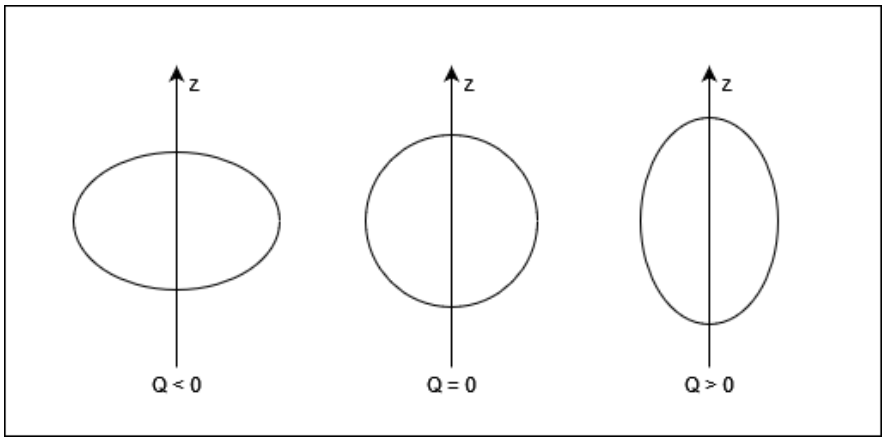

Figure 3 – Shapes of nuclei based on the value of the electric quadrupole moment

Nuclear charge radius Nucleons are confined to an atom's nucleus, but the atomic nucleus does not have a definite outer limit, much like a planet's atmosphere. Instead, nuclei have a function that describes the nucleon density as a function of distance from the center of the nucleus. Assuming a nucleon has a radius of r_0 on the order of 1 fm, then an atomic nucleus composed of A nucleons should follow the ratio $A \approx \frac{\frac{4}{3}\pi R^3}{\frac{4}{3}\pi r_0^3}$. Therefore the nuclear matter radius should be:

$$R \approx r_0 A^{1/3} \tag{6}$$

It is expected that the nuclear charge radius follows the nuclear matter radius. However, significant differences between the two are of particular interest, leading to neutron-dense or neutron-deficient nuclear skins. Novel experiments such as the antiProton Unstable Matter Annihilation (PUMA) project are seeking to investigate the nuclear surface even for short-lived radionuclides using anti-protons and pion tracking in annihilation processes [17].

The charge distribution of a nucleus was first determined experimentally, rather than predicted theoretically, by R. Hofstadter at the Stanford Linear Accelerator Center (SLAC) using electron scattering [18]. They determined that the charge (and nucleon) density can be described to first order by the Fermi distribution:

$$\rho(r) = \frac{\rho_0}{1 + e^{(r-R)/a}} \tag{7}$$

where ρ_0, R, and a are all fitting parameters. This distribution describes well the nuclear charge distribution above $A > 20$ with $\rho_0 = 0.17\frac{Z}{A}\text{fm}^{-3}$, $a = 0.54\text{fm}$, and $R = (1.128A^{1/3} - 0.89A^{-1/3})\text{fm}$.

Measurements of nuclear charge radii, including short lived radionuclides reveal many interesting phenomena, including pairing effects and signatures for shell closures. However, electron scattering experiments are difficult to perform on short-lived radionuclides given their availability in only small samples sizes at dedicated RIB facilities. Instead nuclear charge radii are determined from so-called isotopes shifts which can be measured with high accuracy and precision by laser spectroscopy even for exotic radionuclides, see Section 2.3.2.

2.2 Atomic shell model

Similar to the nuclear shell model, atoms display interesting characteristics around electron shell closures. This model, aptly named the atomic shell model, originally was formulated as part of the Bohr model of the hydrogen atom but has since been formalized under a quantum mechanical framework [19]. There are four quantum numbers that can be used to fully describe an electron in an atom: n, the principle quantum number; l, the azimuthal quantum number, m_l, the magnetic quantum number; and finally s, the spin quantum number.

The principle quantum number denotes the shell of an individual electron. Each shell represents an electron orbit, and can be filled by $2n^2$ electrons. The factor of 2 is a consequence of the Pauli exclusion principle, by which only 2 electrons (one with up-spin and one with down-spin) can occupy the same state.

Within these shells subshells can arise, which can have quantum number $l = 0, 1 \ldots n-1$. The azimuthal quantum number describes the subshell angular momentum $L = (\hbar)^2 l(l+1)$ as well as the shape of the orbital. Traditionally, there are letter equivalents for notation when describing the l quantum number: for the s (sharp) orbital, $l = 0$; for p (principle), $l = 1$; for the d (diffuse) orbital, $l = 2$; and for the f (fundamental) orbital, $l = 3$. From l, we are also able to define the range for m_l, which is $m_l = -l, -l+1, ...0, ..., l-1, l$. The magnetic quantum number defines the orientation of the orbital in a three-dimensional space. Figure 4 demonstrates the shape and orientation of each orbital based on its 3 first quantum

numbers.

The spin quantum number represents a particle's intrinsic angular momentum. The spin can be further broken down into s, the magnitude of the spin, and m_s the direction of the spin. Since an electron is a fermion, s will always be $\hbar/2$, and therefore m_s will either be $-1/2$ or $+1/2$ (down or up-spin respectively), in units of $\hbar$.

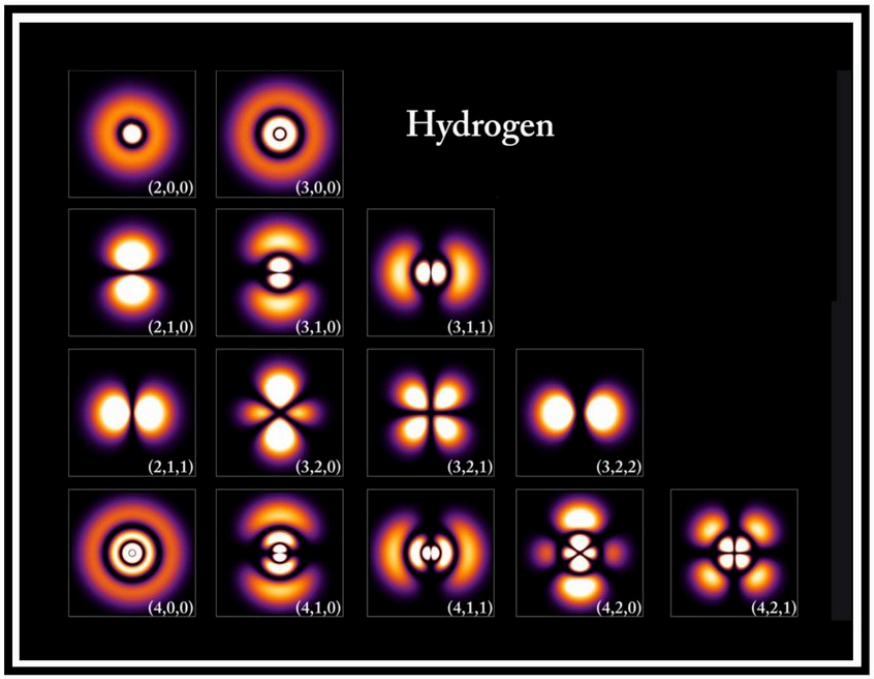

Figure 4 – Hydrogen atomic orbitals visualized. Figure from [20].

2.3 Fine and hyperfine structure

Despite the vast difference between the size of a nucleus and its surrounding electron cloud, the nucleus has significant effects on the atomic orbitals. By studying the atomic structure, researchers are thus able to deduce to a high degree of precision numerous nuclear properties of nuclear ground states and long lived isomers.

2.3.1 Fine structure

To a first approximation, an atom can be modeled as a point charge nucleus surrounded by an electron cloud. When accounting for electron-electron interactions, and hence spin coupling interactions, the total angular momentum of the system can be described as $J =$

$L + S$. The spin orbit interaction causes a shift in energy of:

$$E_{S-O} = \frac{\beta}{2}[J(J+1) - L(L+1) - S(S+1)] \tag{8}$$

where β is the spin-orbit constant dependent on the principle quantum number n and the azimuthal quantum number l [21]. Furthermore, since an electron can have either a up-spin or a down-spin, this creates a splitting of the energy levels with a difference:

$$\Delta E_{S-O} = \frac{\alpha^2}{nl(l+1)} E(n) \tag{9}$$

where $E(n)$ is defined by the Bohr formula $E(n) = -\frac{e^2/4\pi\epsilon_0}{2a_0}\frac{1}{n^2}$ and α is the fine structure constant. This structure is called the fine structure.

2.3.2 Hyperfine structure

However, when taking the internal size and structure of the nucleus into account this causes further shifts and splittings from the expected energy levels, known as the hyperfine structure. It arises from the electromagnetic interaction of the nuclear moments with the orbiting electron cloud. A new quantum number is therefore necessary to characterize the states of this system, the total angular momentum F. This is the vector sum of the nuclear spin I and the total electron spin J; therefore, F can range from $|I - J|$ to $I + J$.

Since there are two electromagnetic moments associated with the nucleus, there will be two contributions to the resulting energy shift.

The first contribution comes from the magnetic dipole moment, μ, described above in Section 2.1.2, interacting with the magnetic field at the center of the nucleus that is generated by the electrons, B_J. Using $C = F(F+1) - I(I+1) - J(J+1)$ as a notation, the atomic energy shift due to the interaction with the nuclear magnetic dipole can be stated as:

$$\Delta E_{dipole} = \frac{\mu B_J}{2IJ} C \tag{10}$$

where $\frac{\mu B_J}{IJ} = A_J$ is defined as the magnetic hyperfine coupling constant. This is only valid for $I > 0$ and $J > 0$ as otherwise there is no hyperfine splitting.

A second contribution arises from the nuclear electric quadrupole moment Q as defined also in Section 2.1.2. Here the contribution only exists for $I, J > \frac{1}{2}$, as otherwise $Q_s = 0$. Here the energy shift is:

$$\Delta E_{quad}/\hbar = B_J \frac{3C(C+1) - 4I(I+1)J(J+1)}{8I(2I-1)J(2J-1)} \tag{11}$$

where B_J is the quadrupole hyperfine parameter defined by $B_J = eQ_s \left\langle \frac{\partial^2 V_e}{\partial z^2} \right\rangle$ [22]. Past first order approximations the contributions of higher order electromagnetic multiples become sufficiently negligible where they can be ignored, and only the magnetic dipole and electric quadrupole moments need to be considered. Once A_J and B_J are known for a reference isotope with known nuclear moments, unknown nuclear moments of other isotopes of a chemical element can be extracted using ratios of the atomic hyperfine coupling constants A_J and B_J of lower- and upper-hyperfine levels:

$$\mu = \mu_{ref} \frac{A_J I}{A_{J,ref} I_{ref}} \tag{12}$$

$$Q = Q_{ref} \frac{B_J}{B_{J,ref}} \tag{13}$$

These ratios are valid all along the isotopic chain, though some smaller order corrections are necessary in μ for some isotopes with significant hyperfine anomalies [23].

In addition to the hyperfine splitting due to the nuclear electromagnetic moments, the atomic nucleus also affects the atomic spectra through its non-vanishing size and charge radius. In particular, the isotope shift $\delta\nu$ reflects tiny differences in (fine structure) transition frequencies when more and more neutrons are added to the atomic nucleus. For the shift between isotope A and another isotope A' of the same element, the difference in transition frequency is:

$$\delta\nu^{A,A'} = \nu_0^{A'} - \nu_0^{A} \tag{14}$$

The isotope shift is the sum of the mass and field shifts, of which the latter is proportional to the differences in mean square charge radii $\delta \left\langle r^2 \right\rangle^{A,A'}$ between isotope A and A'.

2.3.3 Using CLS to probe the hyperfine structure and to extract isotope shifts

The hyperfine structure as well as isotope shifts can be investigated using collinear laser spectroscopy [24]. This experimental technique uses an accelerated ion beam overlapped with a laser to excite the ions to a higher energy level when the laser wavelength matches the energy difference of the selected electronic transition. The ions then emit fluorescence photons, which can be detected by a photomultiplier tube (PMT) in an optical detection region (ODR). To scan the hyperfine spectrum of an isotope, it is necessary to scan the wavelength of the laser in the reference frame of the ion beam. A clever technique can be applied in which the ions are accelerated resulting in a shifted laser frequency (and therefore wavelength).

This can be achieved by taking advantage of the relativistic Doppler effect [25]. In the reference frame of the ions, the laser wavelength will be shifted according to:

$$f = f_L \frac{1 - \cos(\alpha)\beta}{\sqrt{1-\beta^2}} \tag{15}$$

where α is the angle between the ion beam and the laser, and β is the relativistic Lorentz factor:

$$\beta = \frac{v}{c} = \sqrt{1 - \frac{M_0^2 c^4}{(Uq + M_0 c^2)^2}} \tag{16}$$

Here M_0 is the rest mass of the ions, q is the charge of the ions, and U is the total acceleration voltage. In this case, the beam is parallel to the laser so $\alpha = 0$ and therefore the observed frequency for the ions is $f = f_L \frac{1-\beta}{\sqrt{1-\beta^2}}$.

For high-resolution CLS, fast-ion beams are used as a tool to minimize Doppler broadening and thus to obtain a high laser-spectroscopic resolution. The relation $\sigma_f \propto \sigma_E/\sqrt{E}$ indicates that the best results are achieved with low energy spread σ_E and high-energy E beams [26]. Hence, it is advantageous to use fast-ion beams, typically on the order of tens of kiloelectronvolts, paired with a low energy spread.

3 MIRACLS Principle

Far from the valley of stability, isotope production becomes increasingly difficult and thus ions of interest can be synthesized and delivered with yields as low as a few ions per second. Typical CLS setups are limited to nuclides with productions of 1,000-10,000 ion/s delivered to the CLS apparatus depending on the case and employed spectroscopic transition. Moreover, very exotic isotopes are typically delivered with significant contamination from other radionuclides [27]. All these factors make it so that measurements of low-yield nuclides require novel measurement techniques to increase sensitivity and efficiency. The Multi-Ion Reflection Apparatus for Collinear Laser Spectroscopy (MIRACLS) offers a solution to these challenges by performing CLS inside an MR-ToF (Multiple-Reflection Time-of-Flight) apparatus. Following the successful demonstration of the MIRACLS concept in a low-energy MR-ToF device [28–30], a new high resolution setup is currently being built and finalized at ISOLDE, CERN. This new MIRACLS apparatus will offer the ability to trap and measure low-yield nuclides with high experimental sensitivity and high spectroscopic resolution. Additionally, the mass separation capabilities of the MR-ToF instrument will allow the suppression of disturbing contaminants.

3.1 ISOLDE production scheme

Given the short lifetimes of many isotopes of interest, nuclear physics experiments often require on-demand production of isotopes in order to study them. The Isotope Separator OnLine DEvice (ISOLDE) is CERN's facility dedicated to the production and study of radioactive ion beams (RIBs). ISOLDE uses the isotope separation online (ISOL) method, where a high-energy 1.4 GeV pulsed proton beam from CERN's Proton Synchrotron Booster is directed to and impinged onto a thick target. This creates a wide variety of radionuclides via fission, fragmentation, and spallation reactions. The target is kept at a high temperature in the order of ~ 2000°C. This facilitates the diffusion of the synthesized radionuclides into the ionization region, where the radioactive atoms can be ionized via surface, plasma, or resonance laser ionization sources. The ions are subsequently accelerated to an energy of 30 to 60 keV.

Depending on the used target station, the beam is either directed into the General Purpose Separator (GPS) or High-Resolution Separator (HRS), where the ions of interest are selected in mass by passing one (GPS) or two (HRS) magnetic dipole separators [27]. However, these magnets can only separate the beams with a resolving power of $R = m/\Delta m \approx 800$ for GPS and a few thousands for HRS; to further suppress remaining contaminating isobars, experimentalists would often benefit from an additional separation, such as using an MR-ToF device. Beams delivered from HRS are then directed into ISCOOL, the ISOLDE radiofrequency quadrupole trap, where they are bunched and cooled before the beam is sent to one of the various experimental stations at ISOLDE.

ISOLDE is able to deliver beams of over 700 different nuclides, which are used in various experiments in fields such as nuclear physics, life sciences, solid state physics, fundamental symmetry studies, and nuclear astrophysics.

3.2 Using MR-ToF devices to increase CLS sensitivity

Multi-Reflection Time-of-Flight (MR-ToF) devices are primarily employed to perform mass measurements and mass separation. They are used by injecting an ion bunch in between two coaxial electrostatic mirrors separated by a drift tube, and then revolving the ion beam in between these two mirrors. Thus, an effective ion flight path of a few kilometers can be folded into a device with an extension of $\sim 1\,\mathrm{m}$.

The different masses for each ion species in an impure bunch will take different amounts of time to travel in each revolution; after numerous revolutions, the different masses will have formed distinct bunches, which can then be selectively extracted depending on the desired isotope. Assuming uniform kinetic energy E_{kin} upon injection into the MR-ToF device, each mass will have a different velocity:

$$v_i = \sqrt{\frac{2E_{kin}}{m_i}} \tag{17}$$

The mass resolving power is defined as:

$$R = \frac{m}{\Delta m} = \frac{t}{2\Delta t} \tag{18}$$

where t is the total time of flight for the ion species, and Δt is the temporal width of the bunch. Typical MR-ToF devices allow for mass resolving powers greater than $R \sim 10^5$ in only a few (tens of) milliseconds [31–35].

Similar to artificially increasing the distance traveled by the bunch during mass separation, the aim of MIRACLS is to extend the detection region when performing CLS. Ultimately, MIRACLS could achieve tens of thousands of revolutions through the optical detection region, compared to the single pass in conventional CLS. In contrast to other ion traps, an MR-ToF device confines ion bunches of several kiloelectronvolts of beam energy. Thus, by envisioning an unprecedented MR-ToF apparatus operating at 30 keV, the long observation time enabled by an ion trap is combined with the high resolution of fast-ion beam CLS.

3.3 MIRACLS concept

Despite its long and successful history, conventional CLS of bunched beams is limited in its sensitivity to radionuclides with $10^3 - 10^5$ ions per second delivered. Radioactive ions that are available at low energy branches of radioactive ion beam facilities and measured using this techniques have half-lives on the order of milliseconds or more, whereas the ions only interact with the laser beam for a few microseconds at most. By trapping them inside an MR-ToF device and revolving them in-and-out of the ODR, it is possible to extend the interaction time to the order of the half-life, greatly increasing the measurement time and ensuing sensitivity while maintaining the high resolution of conventional CLS.

By extending the interaction time, this results in an improvement in sensitivity of:

$$\frac{S}{N} = \sqrt{r}\frac{s}{n} \tag{19}$$

where S/N is the signal-to-noise ratio of the measurement, r is the number of revolutions in the MR-ToF instrument, and s/n is the signal-to-noise ratio of a single pass through the ODR. Each revolution improves the measurement sensitivity, resulting in an improvement factor on the order of 30 to 700 times compared to traditional, single-passage CLS [36].

However, to achieve this, MIRACLS requires significant changes in the operation of CLS. (1) MIRACLS needs to have a bunched beam of narrow temporal width to ensure effective

MR-ToF operation. (2) The bunch needs to be of sufficient energy to minimize Doppler broadening but with small energy spread to obtain high CLS resolution. (3) Finally, an ODR needs to be implemented into the MR-ToF device directly.

While the MIRACLS concept itself has been successfully demonstrated in a low-energy apparatus with stable ions and a beam energy of $\approx 1.5\,\text{keV}$ [28–30], for online operation, the high resolution setup with up to 30 keV beam energy is required. This high-resolution apparatus requires a newly designed MR-ToF device rated for up to 60 kV applied to the electrodes of its electrostatic mirrors. Additionally, a compact preparation trap for bunching and cooling of the incoming ISOLDE beam is necessary, which must fit in the small space given to the MIRACLS experiment. It must also be rated for a 60 keV beam from the ISOLDE facility.

3.4 First physics cases

The MIRACLS experiment's first physics cases are magnesium (Mg) isotopes in the island of inversion as well as at the $N = 8$ neutron shell closure. Specifically, the experiment will be looking at the nuclear charge radii of ^{20}Mg, ^{33}Mg, and ^{34}Mg in order to validate leading ab-initio nuclear structure calculations. Magnesium was specifically chosen as the first science goal of MIRACLS due to its closed two-level ionic structure in the D1 and D2 transitions (which are the transitions are from the ionic ground state $3s^2S_{1/2}$ to the excited fine structure states $3p^2P_{1/2}$ and $3p^2P_{3/2}$, respectively). With each revolution in the MR-ToF device, the ions are excited and then emit a fluorescence photon; however, if the excited ions were to (partially) decay into a metastable state then the spectroscopic transition could not be re-excited in additional revolutions. By using a closed two-level system, one ensures that the excited ions will decay back into their initial state, therefore allowing the spin-0 isotopes ^{20}Mg and ^{34}Mg to be probed multiple times at MIRACLS prior to radioactive decay. For ^{33}Mg$^+$ ions, the ionic ground state exhibits a hyperfine splitting due to its nuclear spin $I = \frac{3}{2}$. This implies that over time the ions are pumped into other hyperfine states and the MIRACLS signal will eventually diminish. However, MIRACLS' low energy apparatus demonstrated a gain in signal strength by a factor of 5 compared to single-pass CLS even for ^{25}Mg($I = \frac{5}{2}$). Thus, a similar signal enhancement will make a measurement of ^{33}Mg possible, too.

Another element of interest is cadmium, for which experimental studies are planned after successful experiments with Mg isotopes. Cadmium shares the closed two-level property of magnesium, albeit with higher masses, and therefore is ideally suited for performing CLS in an MR-ToF apparatus, too.

Table 1 shows the yields from ISOLDE for the Mg isotopes of interest.

Isotope	**Yield at ISOLDE**
^{20}Mg	17 ions/μC (expected when suppressing ^{20}Na yields) [37]
$^{21-33}$Mg	>1000 ions/μC [38]
^{34}Mg	140 ions/μC [38]

Table 1 – Isotope production yields for ^{20}Mg, ^{33}Mg, and ^{34}Mg in units of ions per μC of proton beam current.

3.5 Overview of MIRACLS beamline

MIRACLS' high resolution setup is presented in Figure 5. Ions delivered by ISOLDE at $\approx 50\,\text{keV}$ will be accumulated and trapped inside the Paul trap that sits on a two-stage high-voltage platform (floated to 48 kV and 50 kV) to match the incoming ion beam energy. This Paul trap serves as a cooler-buncher for the rest of the MIRACLS setup. Ions injected into the Paul trap (floated at the 50 kV high-voltage platform) will be bunched and cooled using room temperature helium gas, after which the bunches will be extracted and accelerated into the 2 kV transport beamline, which is floated to 48 kV with respect to the laboratory ground.

Downstream of the Paul trap there is a quadrupole bender which connects the offline ion source branch to the rest of the beamline. The offline branch is used to provide continuous beam of stable isotopes for setup and system optimization prior to online measurements. The ion source itself is also floated to 2 kV on top of the 48 kV high-voltage platform. Ideally, the offline ion source would have been located upstream of the Paul trap near the hand-over point between ISOLDE and MIRACLS. However, due to space constraints in the ISOLDE hall it was placed after the Paul trap and will require reverse beam injection into the Paul trap. In order to inject into and extract from the Paul trap using the same side, the bias voltages applied to ion optical elements along the shared beam path will need to be switched

from reverse injection to extraction mode during the ion cooling in the Paul trap, on a short timescale of a few milliseconds.

Downstream of the quadrupole bender a 30 degree bender allows for bi-directional laser access into the MR-ToF instrument. Directly following the 30 degree bender the ions leave the 48 kV platform and are accelerated to $\approx$ 50 keV for injection into the MR-ToF device. Finally, at the end of the beamline there is the MR-ToF device itself. It is composed of two large chambers housing the electrostatic mirrors with a drift-tube and ODR in between these two chambers. The ions are captured into the MR-ToF device by means of the in-trap lift technique [39].

Along the entire beamline, the system will have multiple beam optics elements and diagnostics as well: there are double-sided plates directly before and after the Paul trap for tuning through the Paul trap in normal or reverse operation. These can also be used to measure beam transmission through the Paul trap. There is a collimator directly after the offline ion source and a single-sided plate on the quadrupole bender for tuning the ion source branch. In order to detect bunched beams, there is a magneTOF ion detector directly before the 30 degree bender, and two magneTOF detectors in the MR-ToF device, one in each electrostatic mirror chamber. MagneTOF ion detectors are devices that measure ion time-of-flights with sub-nanosecond resolution [40].

There are multiple beam optics components all throughout the beamline to assist with steering and focusing: a high-voltage einzel lens before the Paul trap, two einzel lenses between the Paul trap and the quadrupole bender, an einzel lens in the ion source branch, and another einzel lens directly downstream of the quadrupole bender.

The system also features three gate valves to separate different vacuum sections for system safety. One is installed directly after the Paul trap, one separates the ion source branch, and finally one is installed directly after the 30 degree bender.

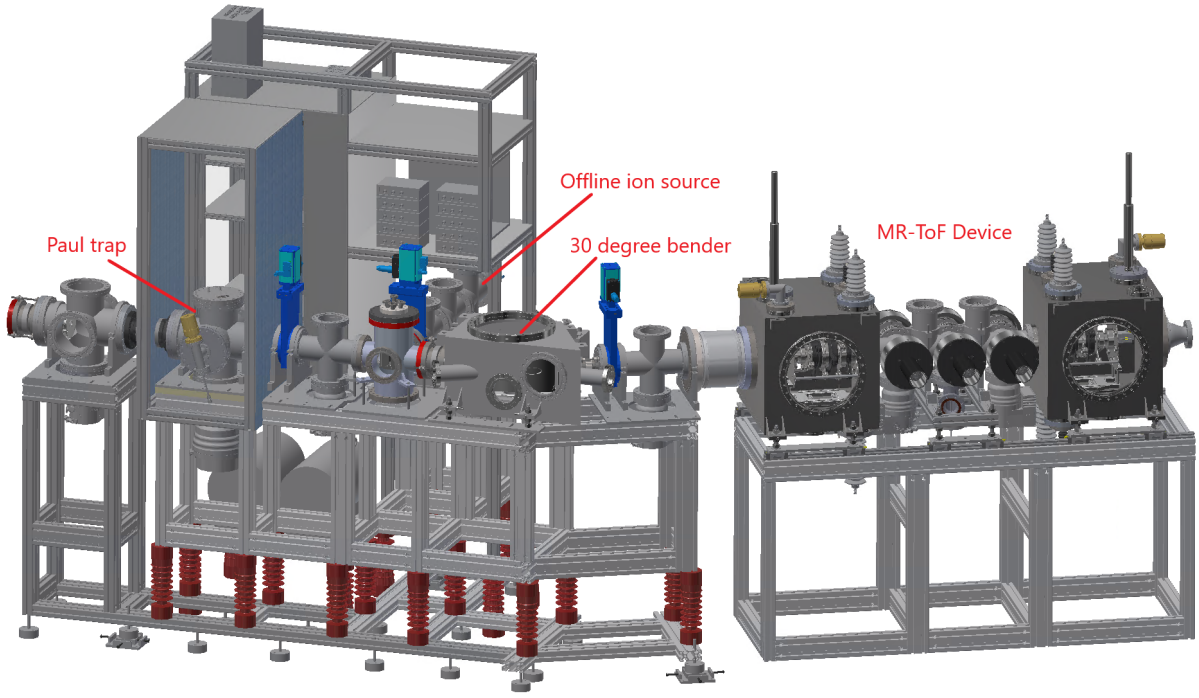

Figure 5 – CAD model of the MIRACLS high resolution apparatus. ISOLDE beam enters from the left.

3.6 Using Paul traps as a cooler-buncher preparation trap

As described in Section 3.3, the MIRACLS technique requires bunches with a small time and energy spread for optimal MR-ToF performance. A small temporal ion-bunch width is needed to fully capture the ion bunch with the in-trap lift and to maintain a short bunch structure during the entire storage time in the MR-ToF instrument. The latter is also beneficial for CLS sensitivity as it allows to gate on a narrow ion-bunch passage and thus to reject more background photons uncorrelated to the ions. Additionally, for CLS a small energy spread on the order $\lesssim 1\,\mathrm{eV}$ is required to decrease Doppler broadening. The quality of a bunch can be described by its longitudinal and transversal emittances, where longitudinal emittance is a product of the time and energy spreads. This concept will be further described in Section 3.6.3.

In order to prepare the continuous ISOLDE beam into bunches for MR-ToF use, MIRACLS uses a newly designed Paul trap. Also known as an RadioFrequency Quadrupole (RFQ) cooler buncher, this device uses a buffer gas to cool the ions while they are being trapped by

an oscillating RF field.

3.6.1 Operation principles of Paul traps

The goal of an ion trap is to confine ions in all three spacial dimensions. However, Earnshaw's theorem states that no point charge can be confined in three dimensions with simply electrostatic fields [41]. A Paul traps gets around this by using rotating electric fields to trap the ions.

This can be easily understood by imaging a ball on a hyperbolic paraboloid surface, as seen in Figure 6. If the saddle surface is stationary, the ball is confined in one direction, but free to fall in the other direction. However, if the field is rotated with a frequency within a specific range, the ball will feel a net force towards the center of the field, be unable to fall in either direction, and will therefore be confined.

The first Paul trap designs were typically made with three hyperbolic surfaces acting as two endcaps and a ring electrode [42]. However, hyperbolic sheets are difficult to manufacture, and such a design restricts accessibility, e.g. for laser access, as well as scalability to larger sizes. As such, linear Paul traps have gained popularity compared to their traditional counterparts. A linear Paul trap functions similar to a quadrupole mass filter. Thus, the hyperbolic field ensures radial ion confinement while the axial trapping is achieved by an electrostatic potential which is formed by DC electrodes and/or endcaps. The radial hyperbolic field is approximated by using four half-cylindrical rods as shown in Figure 7.

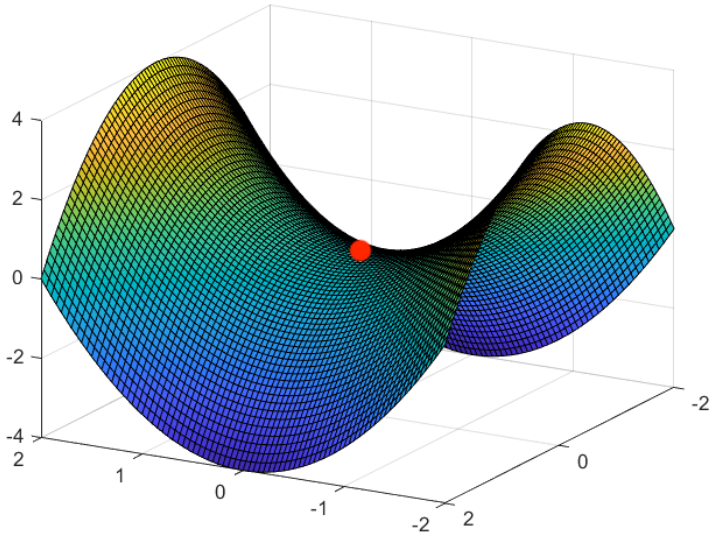

Figure 6 – Ball on a saddle potential. Rotating the potential around its saddle point with specific frequencies will trap the ball in the local minimum of the saddle.

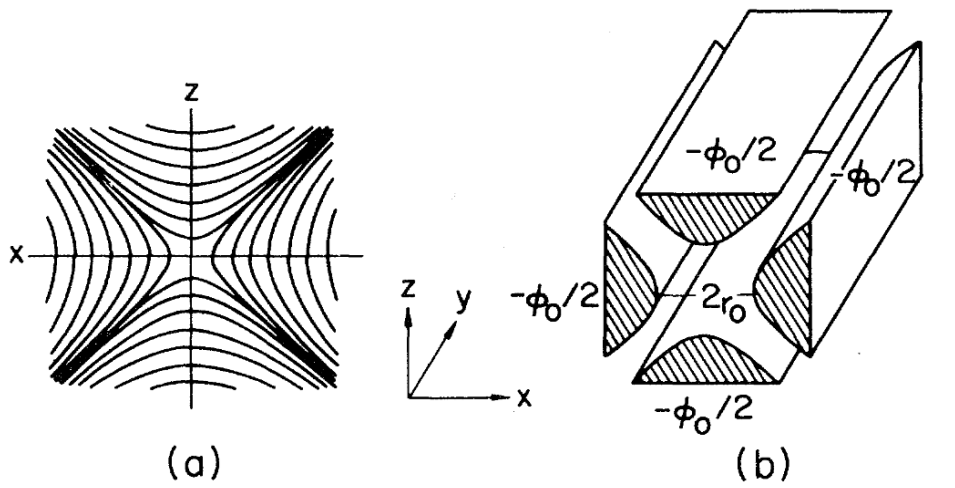

Figure 7 – (a) Hyperbolic field lines generated by applying the potentials on the electrodes seen in (b). Figure from [42].

3.6.2 Mathieu equations and parameters

In this section, z represents the longitudinal coordinate of the Paul trap, while x and y reflect the radial coordinates. The cylindrical rods will generate a potential:

$$\Phi(t) = \frac{V(t)}{2r_0^2}(x^2 - y^2) \tag{20}$$

where r_0 corresponds to half the distance between two opposing rods and $V(t)$ is a time dependent voltage applied to the electrodes [42]. $V(t)$ can either be a sinusoidal wave $V(t) = U + V_0\cos(\omega t)$ or a square wave $V(t) = U + V_0\delta(t)$ with total period T where

$$\delta(t) = \begin{cases} 1 & 0 \leq t < T/2 \\ -1 & T/2 \leq t < T \end{cases}$$

and U is a DC voltage and V_0 is the RF amplitude. The sinusoidal potential can be inputted into the general equation for a Lorentz force acting on a particle in an electrostatic field $F = -e\Delta\Phi$ applied on a quadrupole mass filter [42]:

$$m\ddot{x} = -e\frac{\Phi_0}{r_0^2}x \tag{21}$$

$$m\ddot{y} = e\frac{\Phi_0}{r_0^2}y \tag{22}$$

$$m\ddot{z} = 0 \tag{23}$$

The equations for the x- and y-components can be rewritten as:

$$0 = \frac{d^2x}{d\tau^2} - (a_x - 2q_x\cos(2\tau))x \tag{24}$$

$$0 = \frac{d^2y}{d\tau^2} + (a_y - 2q_y\cos(2\tau))y \tag{25}$$

where $q_{x,y} = \frac{2eV_0}{\omega^2 m_0 r_0^2}$ and $a_{x,y} = \frac{4eU}{\omega^2 m_0 r_0^2}$. These are the Mathieu equations, which have either stable or unstable solutions [43]. Stable solutions are defined as the parameter-space where the motion around the z axis is stable, and radial motion is limited in amplitude. Figure 8 shows the stability diagram for trapping in a linear Paul trap [44]. Since $U = 0$ for the

MIRACLS Paul trap, a will always be zero. For a square wave, optimal q values are between 0.3 and 0.4 but for stable ion confinement can be as high at $q = 0.7$ [45].

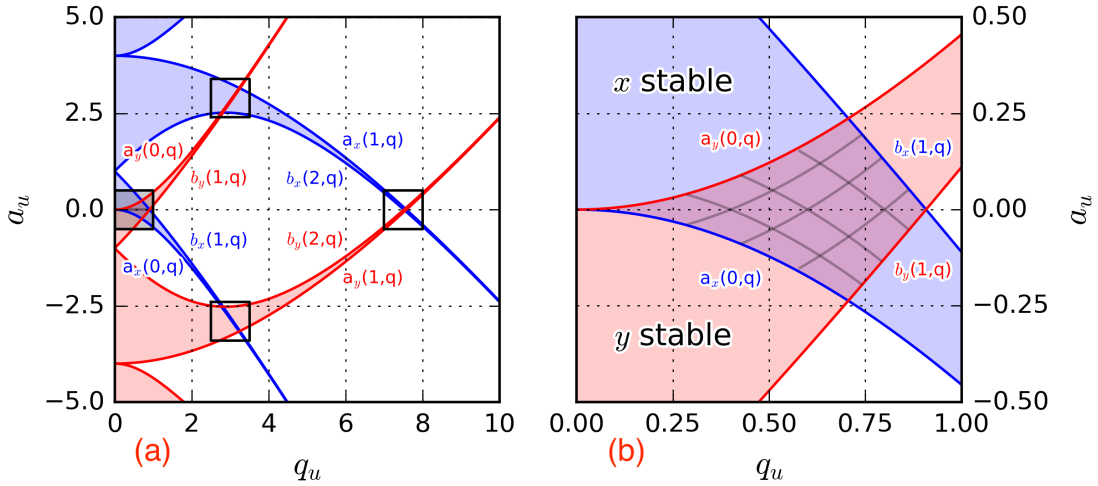

Figure 8 – (a) Stability diagram for a linear Paul trap with sinusoidal RF fields. Stable trapping occurs in the overlapping regions, of which there are four indicated. (b) An enlarged view of the largest region of stability. Figure from [44].

3.6.3 Emittance

As mentioned in Section 3.3, high quality ion bunches are crucial for the MR-ToF operation at MIRACLS. The bunches are evaluated by their emittance, which is a measure of a bunch's (temporal) width, radial extension and divergence as well as energy spread. The emittance can be separated into a longitudinal and transversal emittance.

The longitudinal emittance is a combination of an ion bunch's temporal width σ_t and energy spread σ_E. The root-mean-square longitudinal emittance is defined as:

$$\epsilon_{rms,long} = \sqrt{\langle E^2 \rangle \langle t^2 \rangle - \langle Et \rangle^2} \tag{26}$$

which simplifies to $\epsilon_{rms,long} = \sigma_E \sigma_t$ if E and t are not correlated. For ions in thermal equilibrium with the buffer gas that are subsequently extracted from a Paul trap, the longitudinal RMS emittance of the ion bunch can be estimated [46] according to:

$$\epsilon_{rms,long} \approx \pi \frac{k_B T}{\omega_z} \tag{27}$$

where T is the temperature of the buffer gas and $\omega_z = \sqrt{\frac{2eV_{DC}}{mr_0^2}}$ is the ions' longitudinal oscillation frequency in the Paul trap.

The root-mean-square transversal emittance is defined as:

$$\epsilon_{rms,trans} = \sqrt{\langle u^2 \rangle \langle p_u^2 \rangle - \langle u p_u \rangle^2} \tag{28}$$

where $u = x, y$ is the ions' displacement from the beam axis and $p_u = p_x, p_y$ is their momenta in the transverse directions. Similar to the longitudinal emittance, this can be estimated as a function of the radial oscillation frequency ω_r [46]:

$$\epsilon_{rms,long} \approx \pi \frac{k_B T}{\omega_r} \tag{29}$$

Assuming a Gaussian beam, both RMS emittances can be converted into a measurement of the percentage $p\%$ of the beam that is described by the emittance. For a 95%-emittance, the RMS-emittance can be multiplied by a factor of $2\ln(20)$ [47]:

$$\epsilon_{95\%,long} = 2\ln(20)\epsilon_{rms,long} \tag{30}$$

$$\epsilon_{95\%,trans} = 2\ln(20)\epsilon_{rms,trans} \tag{31}$$

Subject to conservative forces, the emittance is a conserved quantity and thus should not change along the beamline; the exception is inside the Paul trap, where the buffer gas cooling procedure is non-conservative and the emittance is intentionally reduced.

4 Experimental setup

The experimental setup for testing and characterizing the Paul trap has a few variations compared to the final MIRACLS beamline. The biggest difference is the option of operating the 48 kV platform on ground, since the stable beam for the Paul trap commissioning is delivered at ≤ 2 keV from the offline ion source rather than the 60 keV beam from ISOLDE.

4.1 Overview of the present beamline

The experimental setup of the present work contains many components that are permanently installed and will remain part of the full MIRACLS beamline. The beamline built and used in this work is shown in Figure 9.

Magnesium ions are created in the offline ion source, where a collimator is installed to provide a well-defined ion beam and to separate the ion source region from the ultra-high vacuum sections of the transfer beamline. The ion source facing plate of the collimator is electrically isolated and allows to measure the intensity of ion beam fraction which is not passing through the collimator. Its current reading thus provides information about the ion-beam stability.

Downstream of the collimator there is an einzel lens, followed by a gate valve. After the gate valve there is the quadrupole bender; directly behind the bender, in straight continuation of the ion source beam, there is a one-sided plate to measure the incoming ion beam to aid in beam tuning.

To the right of the bender is a set of einzel lenses, as well as a retractable bi-directional current-measuring plate for beam tuning. The next component is another gate valve, after which is the Paul trap. Lastly, the injection cross, enclosing the high-voltage einzel lens and another retractable bi-directional plate, is installed between the trap and the beam port to ISOLDE, but is not directly used in this work.

Extracted ion bunches from the Paul trap will always travel towards the MR-ToF device. Left of the quadrupole bender there is the 30 degree bender chamber; ejected ion bunches will travel straight through the quadrupole bender to impact the magneTOF ion detector installed at the front of the 30 degree bender chamber.

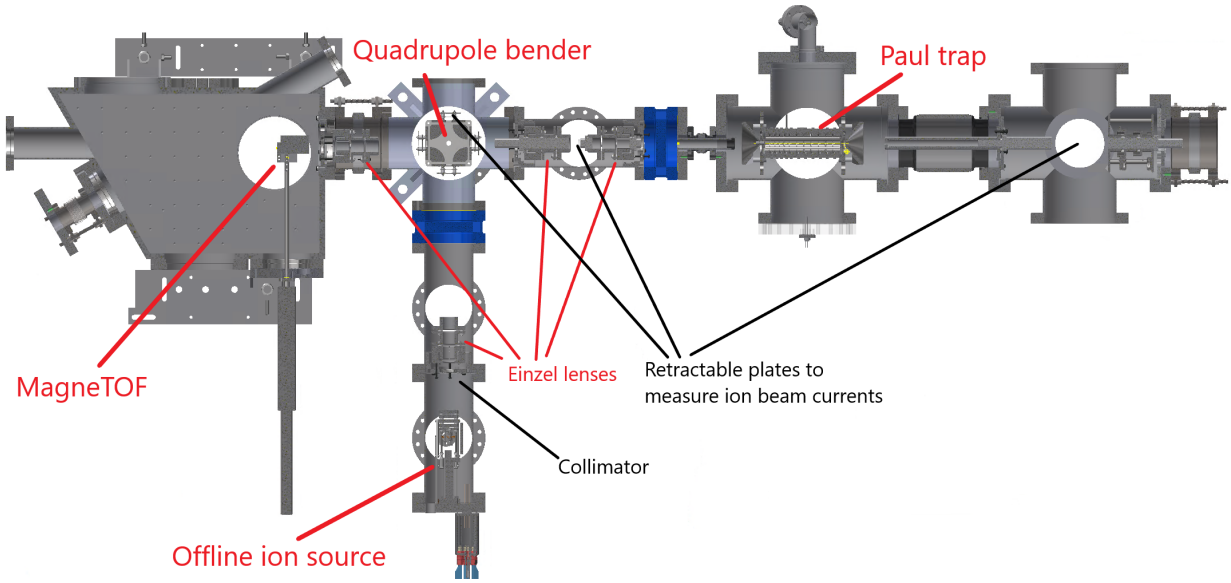

Figure 9 – Overhead view of the Paul trap testing beamline.

4.2 MagneTOF ion detector

In order to measure the ions' time-of-flights precisely, MIRACLS uses a set of magneTOF detectors along the beamline. These detectors are capable of sub-nanosecond ToF resolution, and operate on the principle of secondary electron emission. Incoming ions enter the detector and strike a cathode, which then releases secondary electrons. These electrons are guided by cross electrostatic and non-uniform magnetic fields onto dynodes, which amplifies the measured current [40]. A high voltage, opposite to the ions' charge, is applied in order to power the magneTOF. Figure 10 shows the design and electron path in the magneTOF detector.

In the present work, the magneTOF detector is mounted on a pneumatic actuator, which itself is mounted on a feedthrough flange. This flange has other ports in order to power the magneTOF detector and feed through the measured signal. It is located on the vacuum chamber encasing the 30 degree beam bender.

The signal from the magneTOF detector is passed through an amplifier and a discriminator to convert the analog signal into a digital signal. It is then transported off the high-voltage platform in an optical fibre after converting the discriminator's TTL signal into a light pulse. Finally the signal is fed into the Data AcQuisition system (DAQ).

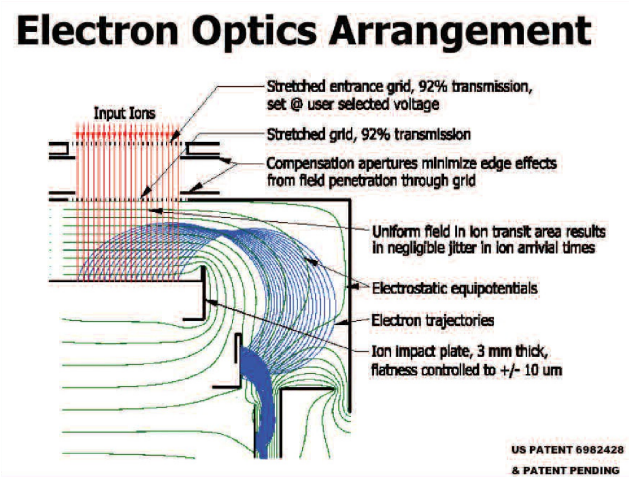

Figure 10 – Ion optical arrangement of the inner magneTOF detector, as well as ion and electron trajectories. Figure from [40].

4.3 Ion source

Access to online ISOLDE beam is limited to due time limitations, so it is of significant advantage to have an offline ion source attached to the beamline. As the element of interest in future online work is magnesium, it is preferred for the ion source to also provide a beam of stable magnesium ions. The ion source used in this setup ionizes the atoms using electron impact ionization. A diagram of the source is shown in Figure 11. An oven filled with solid magnesium is heated to generate the neutral magnesium vapour.

In an electron impact ion source, electrons hit a neutral atom, and, if the kinetic energy of the initial electron exceeds the first ionization energy of the atom, knocks off an electron leaving behind a positively charged ion. The electrons are emitted by a heated filament, and then accelerated towards a grid surrounding the relevant ionization region; the electron energy is determined by the potential difference between the filament and the grid. Its value is set to maximize the formation of Mg^+ ions while minimizing the ionization of other residual-gas particles whose ionization cross sections peak at higher electron energies. After the atoms have been ionized, they can be extracted in a continuous beam. The ion source also has three electrodes in the extraction region for beam focusing. For the stable beams in this study, the grid was biased to +265 V for a beam energy of 265 eV, and the filament biased to +184.3 V which results in an electron energy of $\approx$ 80 eV.

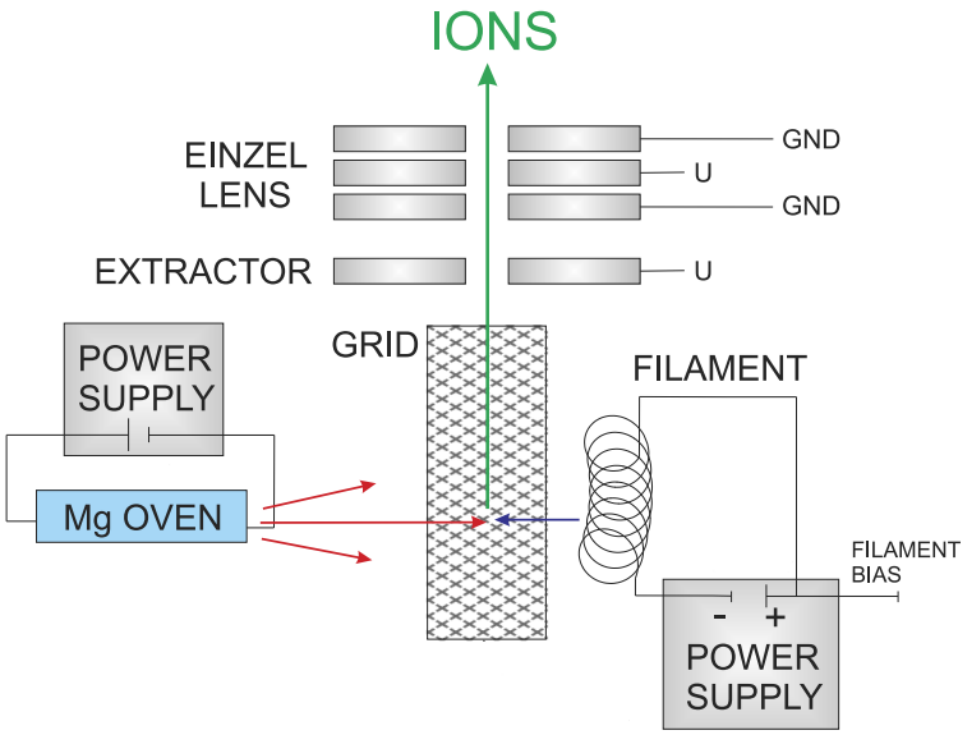

Figure 11 – Diagram of the Mg electron impact ion source used for offline testing and calibrations. Figure adapted from [48].

4.4 Paul trap

Within MIRACLS, the Paul trap is one of the most important components, as it is responsible for preparing the bunches to be injected into the MR-ToF apparatus. The principle goal of this thesis project was to build the test setup as well as to characterize the Paul trap in its first commissioning experiments.

4.4.1 Paul trap requirements

The newly designed Paul trap has stringent requirements for optimal performance. First, it needs to accept and trap ISOLDE beam with minimal ion losses. The MR-ToF device requires bunches with small temporal width ($< 700\,\text{ns}$) while CLS requires bunches with low energy spread ($< 1\,\text{eV}$) and benefits from higher energies [36, 49]. The spacial expansion of the bunches in transverse directions should also be small as to maximize ion-laser overlap. Experimentally, it requires specific devices to measure the energy-spread as well as transverse

displacements and momenta and therefore to obtain the complete phase space. However, through the use of an ion detector the temporal spread of a bunch can be measured, and therefore the Paul trap parameters can be optimized for minimizing the bunch width. The excellent agreement of the measured and simulated ion-bunch structure in the other Paul trap operated at MIRACLS [28] provides strong confidence to gauge the experimental performance of the trap based on the temporal ion-bunch profile and rely on simulations for the other emittance parameters.

4.4.2 Paul trap design

A longitudinal view and an angular cross-section view of the Paul trap are shown in Figure 12. The longitudinal view shows the DC electrode configuration of the Paul trap, as well as the placement of the half-cylinder RF rods. The helium line to supply the buffer gas is visible below the Paul trap, and the D-sub connector to bias the DC electrodes is also visible on top of the trap structure.

The DC electrodes serve to form an axial potential well in the Paul trap into which the injected ions are accumulated. In order to have more control over the well minimum, the electrodes come in two sizes: seven larger electrodes are located at the front of the trap, and five axially shorter electrodes towards the downstream section of the trap to control the field more precisely. The DC electrodes are also manufactured with wedges (which can be seen in Figure 12) which serve to strengthen the static field that is otherwise shielded by the RF rods. The DC electrodes are designed such that the insulating ceramics are never directly exposed to the trapping region; this ensures that any stray ions are unable to impact the ceramic which could otherwise cause a charge build up, and thus uncontrollably alter the electric field seen by the ions.

The RF rods and DC electrodes are sandwiched between two endcap electrodes with a hole with a diameter of 5 mm. By applying the respective potential to the endcaps, they can either confine the ions inside the trap or allow for injection or extraction. On each endcap there is an endcone mounted towards the exterior of the trap. The endcones assist during injection as they decelerate the beam and help focus the ions into the trap. The endcaps also help keep the high pressure buffer gas from increasing the pressure in the rest of the system

by forming a pressure barrier.

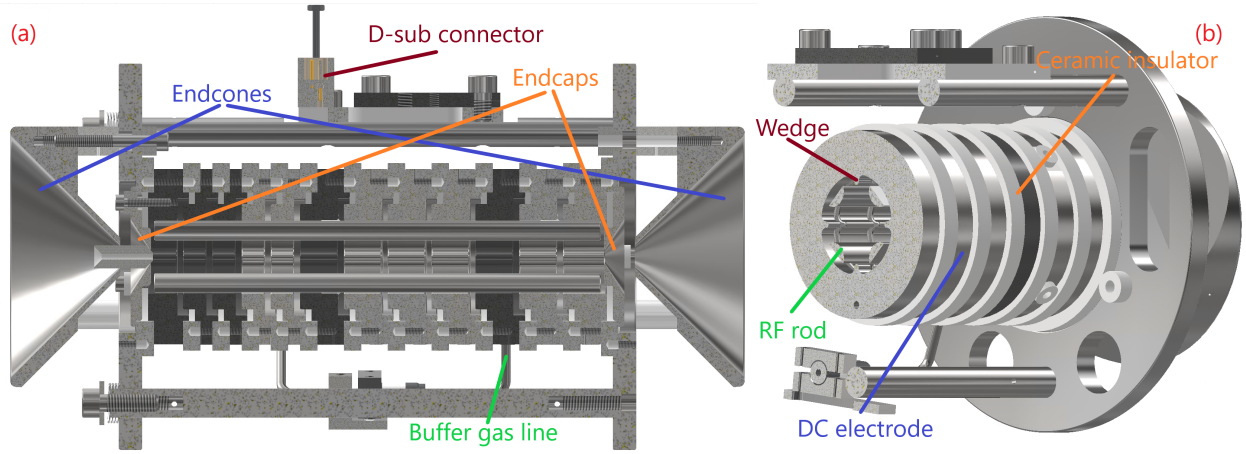

Figure 12 – (a) Longitudinal cross-section of the Paul trap showing the DC electrodes and RFQ cylinders (b) Angular cross-section of the Paul trap showing the spacing between the half-cylinders, and the wedges on each DC electrode as well as the ceramic insulators.

The performance of the Paul trap has been studied in detail through simulations in order to understand the injection from ISOLDE into the Paul trap [50] and its operation within MIRACLS, particularly when trapping a beam from the offline ion source [51].

4.5 Operational details

An important part of the Paul trap operation is the high-voltage platform it sits on. ISOLDE can deliver beam with energies up to 60 keV and the MIRACLS ion trap system is designed to handle incoming ion beams with energies of up to 50 keV in order to maximize the MR-ToF performance. However, due to the space limitations at ISOLDE the setup is very compact. Therefore the Paul trap, with a length of 25 cm, is quite short compared to other cooler-bunchers at RIB facilities. Simulations in [50] indicate that this Paul trap length and its He stopping power is sufficient to efficiently capture a continuous beam of $^{20-34}$Mg ions. For heavier Cd isotopes, ISCOOL may be used as a pre-cooler and buncher such that the ion beams from ISCOOL can be dynamically captured at the MIRACLS Paul trap by closing the injection endcap once the bunch has entered the trap.

Moreover, the ion beam transport from the Paul trap to the MR-ToF instrument is done at $\approx$ 2 keV to allow the use of compact steerers and einzel lenses (compared to lengthy

quadrupole triplets at higher transport energies) before the beam is accelerated back to 50 keV again. For this reason, a two stage high-voltage (HV) platform is installed.

Figure 13 shows a diagram of the control system for the experimental setup. The system is operated using the Experimental Physics and Industrial Control System (EPICS), a set of open-source software developed for the purpose of controlling complex systems from one unified set of tools. This server managing this system is hosted on the Ground Control PC, and will provide a consolidated interface to manage almost all the system parameters. These parameters include: reading out pressure gauges; controlling the Paul trap and beamline tune via the RF power supply, switch and ISEG power supplies; and setting timing patterns.

The utilization of EPICS to control the system has many advantages. As all the parameters are controlled via a server, the MIRACLS beamline can be controlled entirely remotely when radionuclides are delivered from ISOLDE; this is critical, as the high-voltage platforms that are an integral part of the functionality make manual control unfeasible, not to mention exposure to radiation during online radioactive beams studies.

In order to communicate with the EPICS server on ground potential, the high-voltage platforms are equipped with network switches and fiber-to-ethernet converters, and fibres are fed onto the platforms from ground; TTL-to-optical pulse converters are also installed to accomplish the same goal, but with timing pattern signals. The network switches propagate the ethernet connection to the electronics on each high-voltage platform. A WAGO digital-to-analog and analog-to-digital converter is installed to control analog signal devices, which inputs and outputs signals to communicate with pressure gauges, the helium buffer-gas mass flow controller, beamline actuators, and gate valves. An ISEG crate is positioned on each platform to provide bias voltages for the beamline elements. These power supply units come with EPICS pre-installed and are directly connected to the network switch. A PC (with EPICS installed) positioned on each platform controls the remaining devices such as the RF control supplies, picoammeter, and high-voltage Spellman power supply.

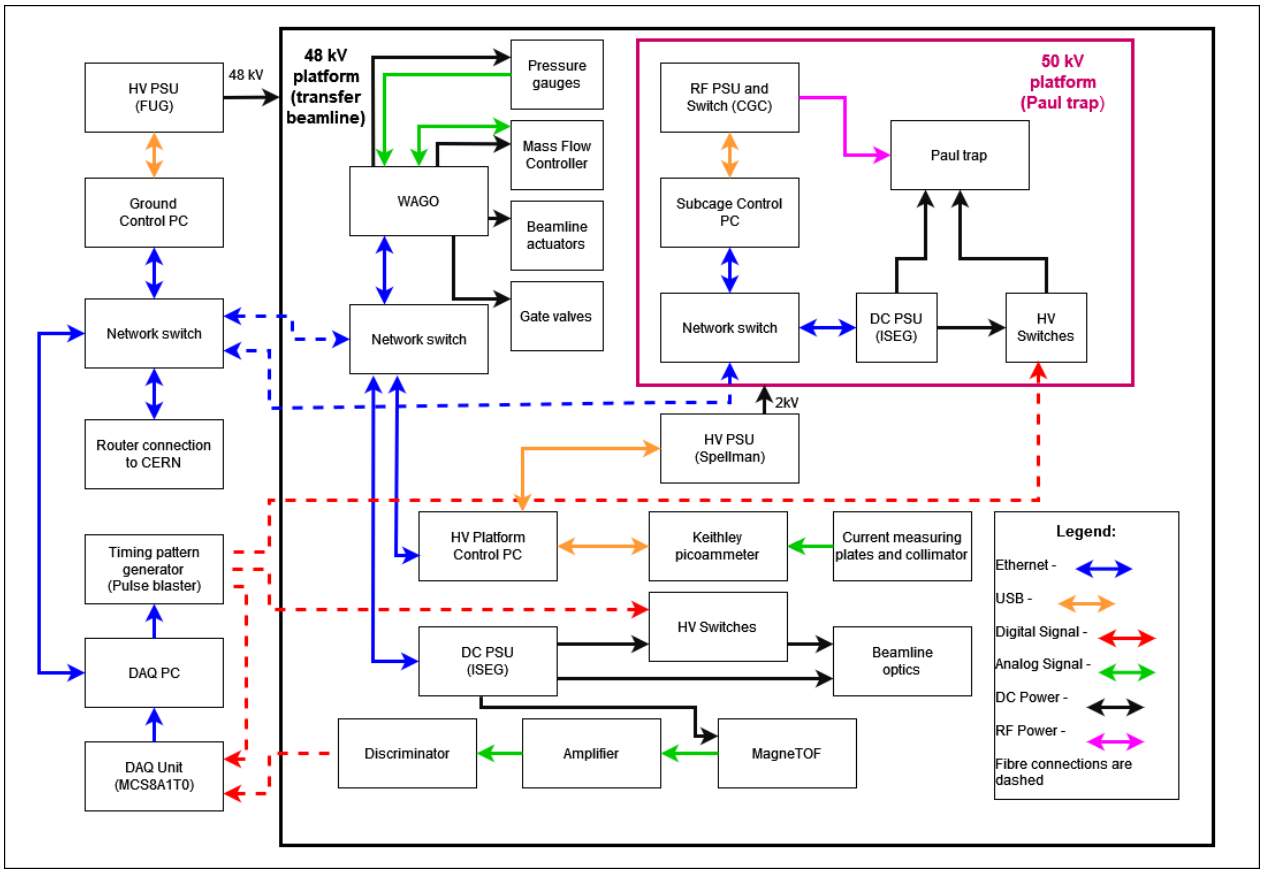

Figure 13 – Control system schematic for MIRACLS.

4.5.1 High-voltage platforms

Most of the MIRACLS transfer beamline between the Paul trap and MR-ToF instrument sits on the first-stage of the high-voltage platform, which is designed to be floated at 48 kV. All beamline components except for the MR-ToF device, reacceleration region, and first vacuum chamber connecting to ISOLDE are located on this platform. The Paul trap itself sits on the second-stage of the platform, which is floated 2 kV on top of the first stage. Floating the Paul trap to close to 50 kV allows one to slow the ions delivered from ISOLDE to a kinetic energy of a few electronvolts before entering the Paul trap. This makes the trapping more effective since the ions now travel through the Paul trap more slowly, therefore interacting more with the buffer gas, and have less energy to dissipate. A simplified circuit diagram of the high-voltage platforms and electronics is shown in Figure 14.

Both of these high-voltage platforms are fully surrounded by perforated aluminum sheets,

and can be accessed through interlocked doors. On the platforms there are a variety of electronics that need to be powered to operate the MIRACLS ion-trap system. In order to provide sufficient electrical power to both platforms across the floating potentials, the system uses isolating transformers that are rated for high voltage differentials. The resistors and capacitor between the platforms serve to safely discharge the platforms when the high-voltage is removed.

In order to fully isolate each part of the voltage platform, ceramic breaks were installed on either side of the Paul trap. Each break contains a grounding tube, which serves to shield the ion trajectory from external fields and to protect the ceramic from building up a charge from ion deposits. A large $\approx 10\,\text{cm}$ long vacuum ceramic break (rated for 60 kV voltage potentials) is installed directly upstream of the Paul trap, and a much smaller $\approx 2\,\text{cm}$ vacuum ceramic break (rated for 10 kV voltage potentials) is installed directly downstream of the Paul trap. The breaks need to be sufficiently long to avoid violent electric discharges that can occur across high-voltage potentials.

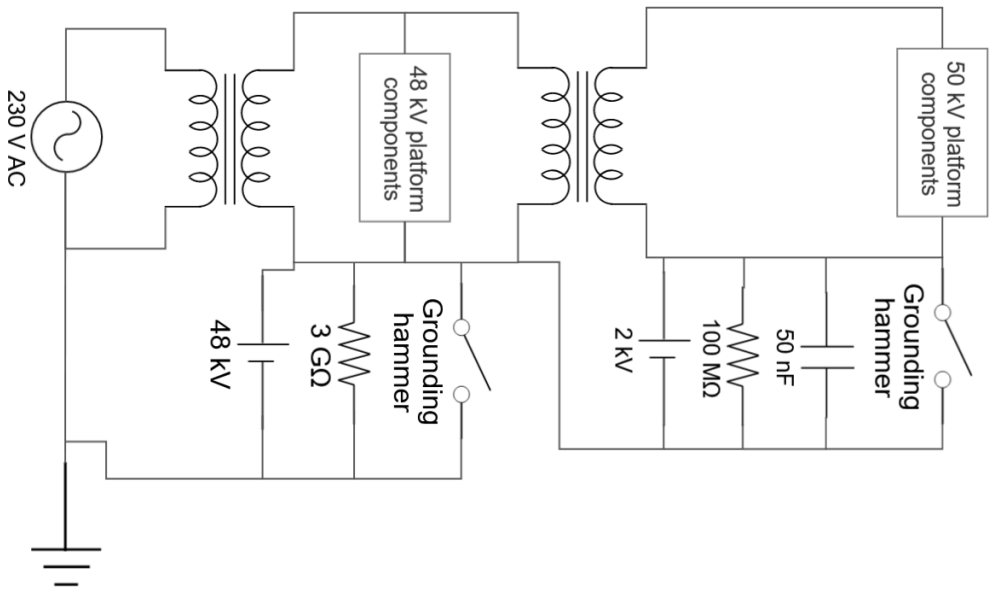

Figure 14 – Simplified circuit diagram of the electronics setup for the final MIRACLS experiment. The switches represent pneumatic hammers that ground the platforms to earth when the safety cage is not locked.

4.5.2 Paul trap operation

The Paul trap is a complex device in this experimental setup. It has a series of electrical components and a gas system, all installed on a high-voltage platform. The Paul trap floating is powered by a Spellman power supply, controlled by a WAGO unit installed on the 48 kV platform, see again Figure 13.

The square-wave RF field is generated by two signal generators to power the cylindrical rods. The Power Supply Unit (PSU) is responsible for outputting the DC voltage and feeds into the voltage switch, which outputs two square waves with opposite phase. Both of these units can be addressed via a USB connection with a control computer placed on the 50 kV subcage HV platform. Some of the DC electrodes are equipped with the ability to switch their electrostatic potential quickly in order to control the ion injection and extraction.

The helium injection system sits entirely off of the high-voltage Paul trap platform. A Grade 5.7 helium bottle is attached to a mass flow controller, which is also controlled via the WAGO unit.

Figure 15 shows an example of the electric potential along the Paul trap axis, one for trapping and cooling the ion beam (blue) and one for extracting the bunch from the trap (red). These electrodes are controlled by HV switches, triggered by a signal sent via a fibre optical cable, which receive the respective bias voltages from an ISEG crate[1]. Figure 16 shows the typical timing pattern which is used during the present Paul trap commissioning with MIRACLS' own ion source.

The measurement cycle starts with the beamline being prepared for ion injection. The beam can enter the Paul trap over the raised potential of the end cap (blue curve in Figure 15). The ions lose energy via collisions with the buffer gas and cool to the bottom of the well. Figure 17 shows the individual steps in the trajectory of the ions through the beamline for offline ion source beam.

After a well-defined ion loading time, a beam gate is enabled by switching the potential of a steerer in the ion source branch to deflect the ion beam away. As no further "hot" ions are injected into the Paul trap, all trapped ions thermalize with the buffer gas. During this

1. Buffer circuits between the ISEG power supply and HV switches were installed in order to minimize noise when switching the electrode potentials rapidly.

cooling time the transfer beamline is prepared for ion transport and ToF measurement at the magneTOF ion detector. Once the cooling time is completed, the Paul trap extraction endcap is lowered (see red curve in Figure 15) and the ions are released. This is also the start signal sent to the DAQ system to measure the ions' time-of-flights until they impringe onto the magneTOF ion detector.

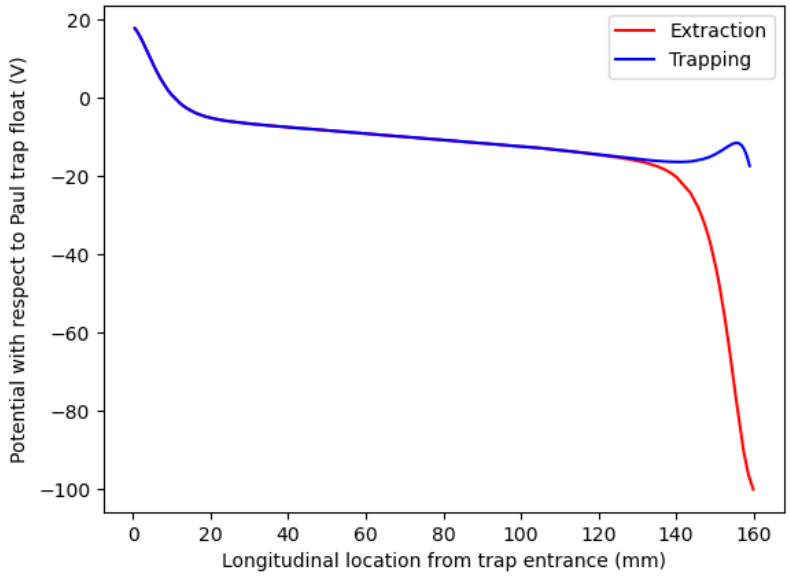

Figure 15 – Example of a potential along the Paul trap axis for trapping ions (blue) and extraction ions (red) in respect to the floating of the Paul trap's cage floating

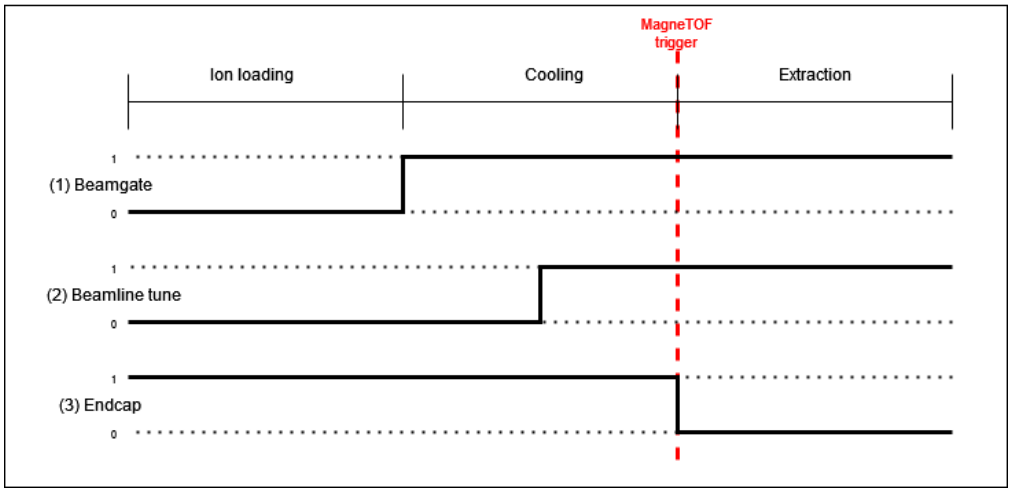

Figure 16 – Timing patterns for the beamgate, beamline tune, endcap switching, and DAQ system trigger

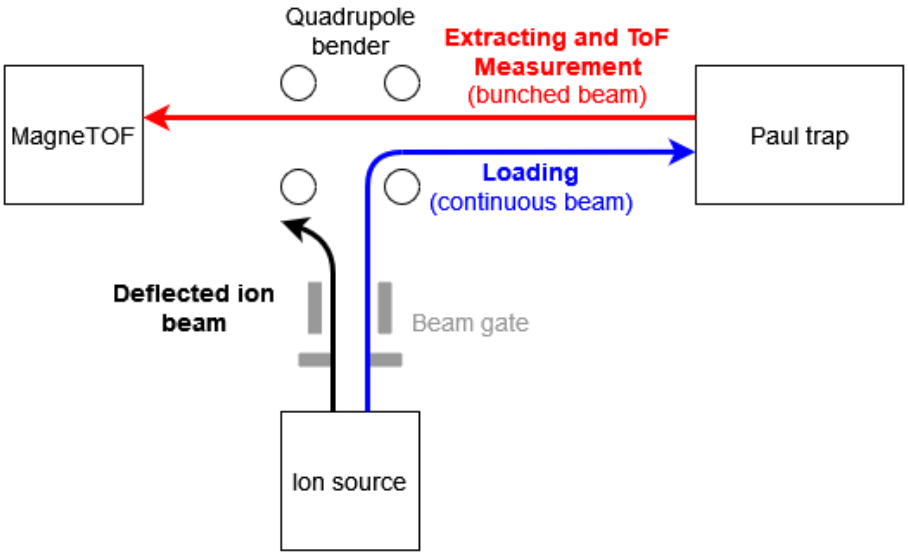

Figure 17 – Schematic of the offline ion source beam trajectory through the beamline. The beam gate is one of the electrodes on the einzel lens steerer in the offline ion source branch.

4.5.3 Vacuum system

Ion trap experiments demand for excellent vacuum conditions to minimize the risk and negative impacts due to ion collisions with residual gas particles. These vacuum requirements are especially stringent in the MR-ToF apparatus to minimize ion losses during the measurements. However, due to the buffer gas cooling, the interior Paul trap pressure required ($10^{-4} - 10^{-2}$ mbar) in order to stop ions is much higher than the pressure desired in the rest of the system ($10^{-9} - 10^{-8}$ mbar). This represents another design challenge, which was solved using differential pumping barriers such as the endcaps, and a multitude of turbopumps installed throughout the system.

Even though the buffer gas pressure is high during operation, the cleanliness of the Paul trap, especially of the trapping region, is imperative. Excessive outgassing or impurities in the gas may lead to charge exchange and thus to undesired ion losses. Great care was thus taken to prepare and assemble the trap as cleanly as possible. Without gas leaking into the trap, the pressure in the Paul trap's vacuum chamber is measured as low as 4×10^{-10} mbar.

Figure 18 shows the planned final vacuum system, including the installed MR-ToF device chambers. For system safety, there is a EPICS-based software interlock that communicates

with the pressure gauges, gate valves, and electrical valves to ensure that any malfunctions close all valves to avoid damage to the vacuum pumps.

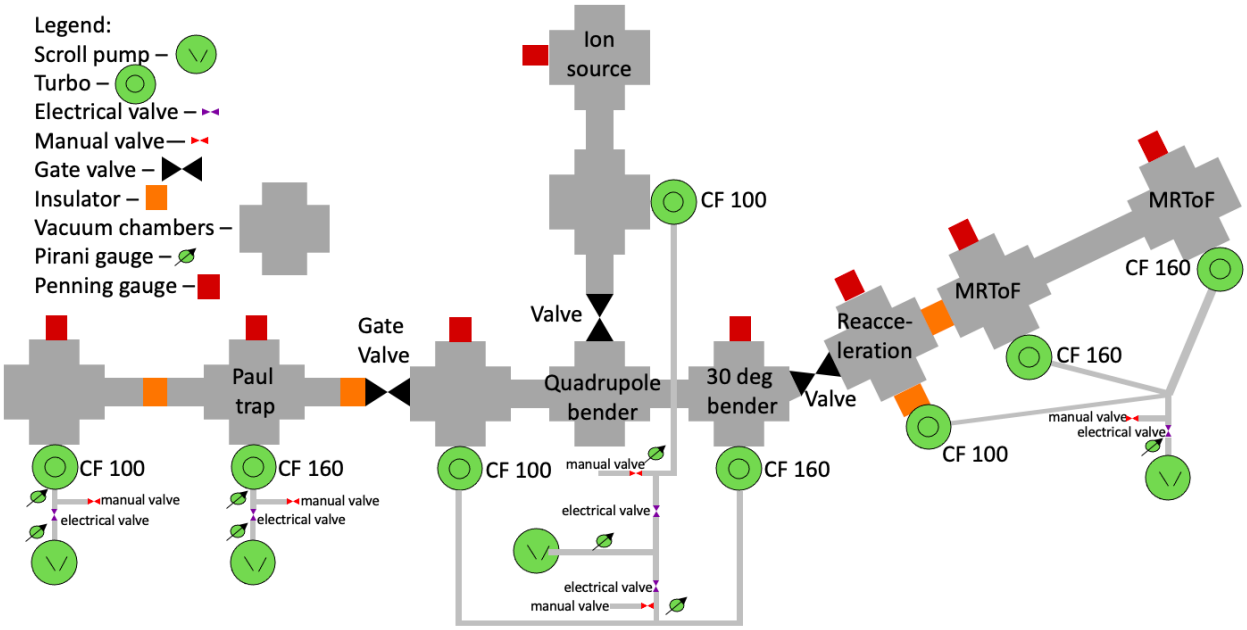

Figure 18 – Diagram of the MIRACLS vacuum system.

5 Experimental results and discussion

5.1 ToF Spectrum of ions extracted from the Paul trap

When the ions are released from the Paul trap, their bunch structure can be characterized by measuring the time of flight (ToF) to a magneTOF ion detector located in the vacuum chamber hosting the 30 degree bender. Whenever an ion from the bunch impacts the magneTOF detector, a signal is sent from the device to a Multichannel analyzer, controlled by MPANT software. The combination of the magneTOF's small signal width of about ~ 1 ns and a data acquisition system capable of resolving signals with 80 ps bins leads to a high time resolution. A typical measurement includes 1000 bunches, also referred to as ion shots or measurement cycles, each lasting around 100 ms.

A sample Time-of-Flight (ToF) spectrum for one measurement is presented in Figure 19.

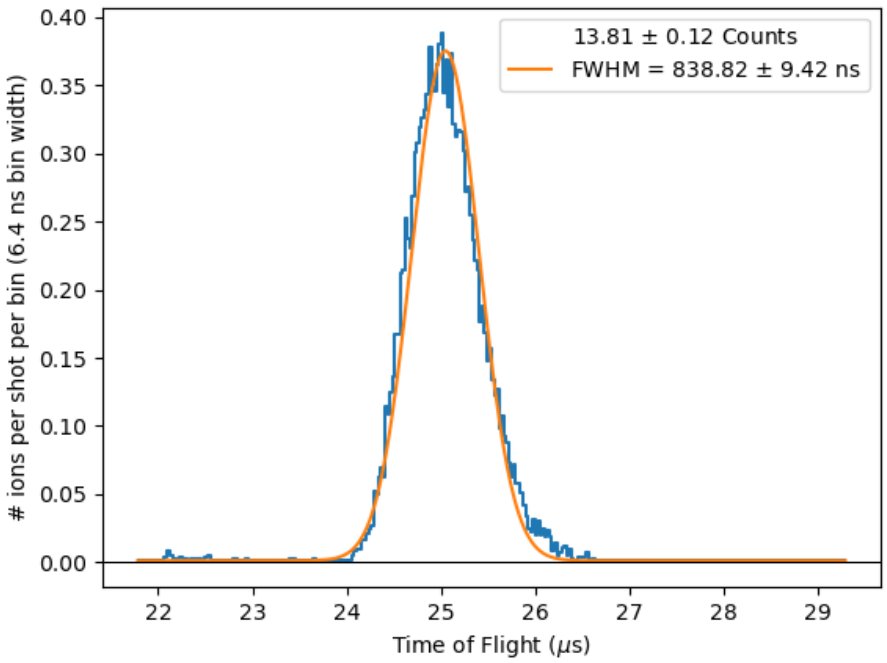

Figure 19 – Example ToF spectrum for a bunch, and the Gaussian fit results. The plotted data represents an average of 1000 cycles. This example has an average of 13.81 ± 0.12 ions per bunch (obtained by integrating the plotted data), with the fit calculating a temporal ion bunch width of 838.83 ± 9.42 ns.

The average number of ions per bunch, also called the counts per shot, can be calculated by numerically integrating the number of ion counts over the bunch spectrum. The total area under the curve is integrated and divided by the total number of cycles to obtain the number of ions per bunch. It is important to trap ions as efficiently as possible, since the yields of the isotopes of interest for MIRACLS are small and any losses are detrimental to the experimental sensitivity. For the same incoming ion flux, it is thus desirable to extract as many ions as possible of the initially injected ions. The number of extracted ions is consequently one measure to characterize the performance of the trap.

As discussed in Sections 3.6.3 and 4.4.1, a measure of the quality of the bunches is the temporal ion-bunch width. It can be characterized by the Full-Width Half-Maximum (FWHM) [2] of a bunch width which can be extracted by fitting the spectrum to a Gaussian distribution, as shown in Figure 19. The bunch center can also be extracted from this Gaussian fit; while the center does not reveal much about the quality of the bunch, it is a useful quantity to know when calibrating the timings along the beamline, such as setting ToF gates at specific moments to select the desired ion species.

As an example, the spectrum shown in Figure 19 is based on data collected over 1000 measurement cycles. The ion bunch contains on average of 13.81 $\pm$ 0.12 ions per bunch, and the fit returns a temporal ion bunch width of 838.83 $\pm$ 9.42 ns (FWHM).

While the Gaussian fit appears overall as reasonable, it has a reduced chi-squared of $\chi^2_r = 2.97$. This is largely due to an apparent skew where the right-side has a more pronounced tail compared to the left-side of the bunch. Magnesium has three stable isotopes with varying abundances: ^{24}Mg(79%), ^{25}Mg(10%), and ^{26}Mg(11%) [52]. Given the short distance between the Paul trap and the magneTOF, these individual isotopes cannot be resolved and thus the less abundant, more massive isotopes lead to a tail with longer time-of-flights. This tail may also be an effect of reheating during the bunch extraction from the trap, in which the accelerated ions collide with the helium gas atoms outside of the Paul trap which spreads the ion energy [53]. This effect will be investigated later in the discussion in Section 5.4.

2. The FWHM is invariant to normalization of a Gaussian distribution.

5.2 RF Stability

The most important parameters for trapping the ions in the Paul trap are the RF amplitude and frequency. The potential generated by the digital voltage on the RF electrodes is responsible for radial confinement inside the Paul trap and is critical in guiding the ions to the axial center. For example, the importance of the RF field is illustrated when sending an ion beam from the offline ion source at low energies ($\leq$ 200 eV) and in continuous mode through the Paul trap; without the RF field applied, ions cannot be seen shooting through the Paul trap.

Figure 20 shows the number of ions per bunch as a function of the RF parameters. A red line showing the theoretical limit for trapping is shown on the left, although the efficiency significantly decreases before this limit. In general, the trap performs best at higher frequencies and voltage amplitudes. However, due to the short distances between the RF electrodes ($\approx$ 1 cm), higher voltages can lead to sparking between the electrodes. During the simulation and design phase of this trap, it was shown that the trapping efficiency initially doubles as the RF amplitude is increased from 50 V to 100 V, but then only slowly improves until it saturates at 200 V [51]. The trap was chosen to run at an RF amplitude of 200 V, and the RF frequency chosen to maximize ion trapping efficiency given this voltage.

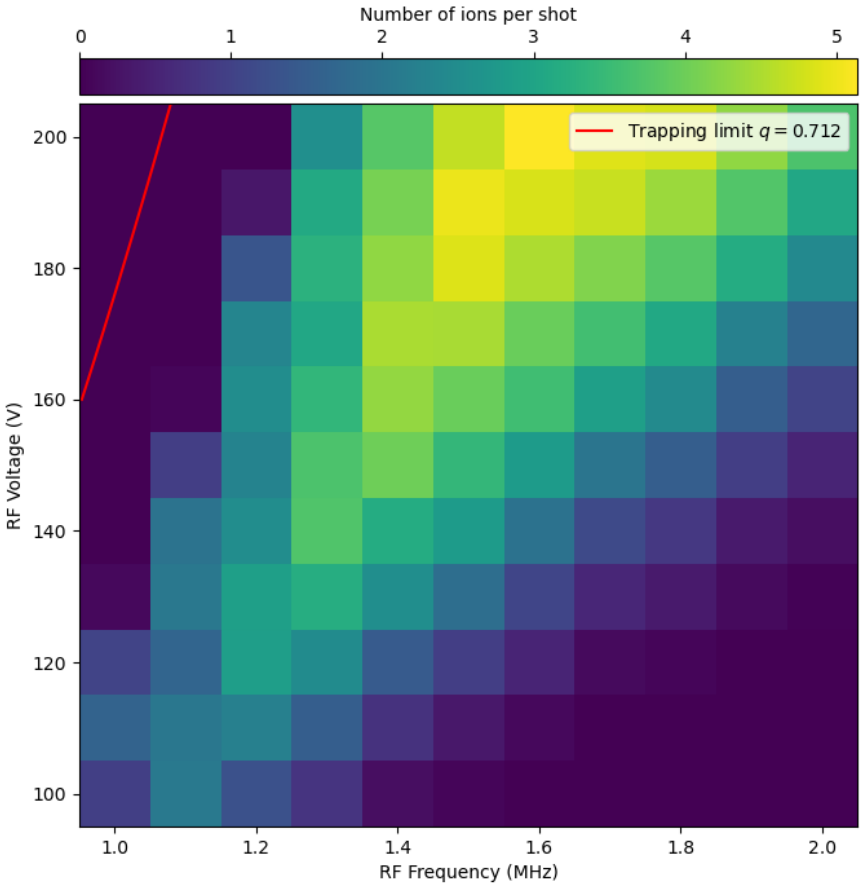

Figure 20 – Measured ions per shot as a function of RF parameters. The theoretical limit $q = 0.712$ is shown as a red line. Experimental parameters: RF parameters = variable, Paul trap floating = +260 V, loading time = 50 μs, cooling time = 30 ms, buffer gas pressure = 3.2 $\times 10^{-4}$ mbar, Endcap and endcone voltages during extraction = -250, -300 V in respect to its HV cage

5.3 Cooling times

Another important parameter of the trap is its cooling time before extraction. During injection, ions entering the Paul trap encounter the potential well formed by the DC electrodes; however, these are electrostatic components and thus do not change the total energy of the ions. In order to decrease the energy and energy spread of the ions, a buffer gas is leaked into the trapping volume. Collisions between the neutral gas and ions decrease the bunch's energy and energy spread. As shown in Figure 16 and discussed in Section 4.5.2, the time between when the beam gate bias that deflects the incoming beam is increased and

endcap bias is lowered to release the ions is referred to as the cooling time, i.e. the amount of time all the ions will interact with the buffer gas before extraction. As the cooling time is increased, the energy and time spreads are expected to decrease exponentially before hitting a saturation limit [54].

Figure 21 shows an ion intensity plot versus ToF and cooling time (a), as well as the counts per shot and ion-bunch width as functions of the cooling time in the trap (b).

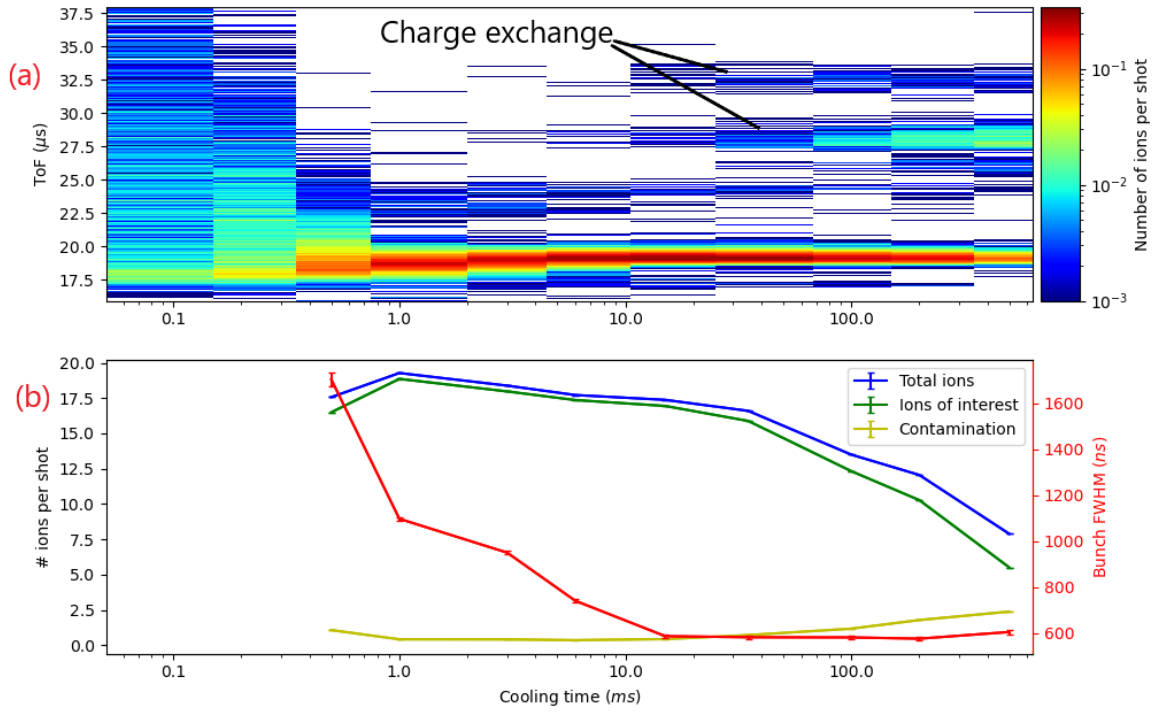

Figure 21 – (a) Ion intensity versus ToF and cooling time. (b) Counts per shot and temporal ion bunch width as functions of cooling time. Experimental parameters: RF parameters = 200 V amplitude, 1.6 MHz, Paul trap floating = +260 V, loading time = 50 μs, cooling time = variable, buffer gas pressure = 3.2 $\times 10^{-4}$ mbar, Endcap and endcone voltages during extraction = -250, -300 V in respect to its HV cage

The lower plot labeled (b) shows the relationship between the ions per bunch and cooling time, and the bunch width and cooling time. The decrease in bunch width as cooling time increases is clearly visible in the plot, as the bunch width decreases steadily before the saturation point at 10 ms cooling time. For a buffer gas pressure of $p \approx 3.2 \times 10^{-4}$ mbar, this results in a total reduction of more than 60% in the FWHM from its initial value and

experimentally demonstrates the effect of the buffer gas cooling.

The upper plot, labeled (a), shows the recorded ToF spectra as a function of cooling time. Once more, the process of ion cooling can be seen in this figure until a narrow but intense central bunch is formed which is centered around 19 µs in ToF. Additionally, there are two smaller bunches at 29 and 32 µs which grow in intensity for longer cooling times. These smaller bunches are indicative of charge exchange, an effect where the ions of interest interact with contaminating residual gas in the trap and transfer an electron from the initial neutral gas particle to the ion of interest. Upon extraction, this contamination will appear as distinct bunches on the magneTOF detector. Since longer cooling times lead to more charge exchange, these bunches grow in intensity with longer cooling times.

There are two potential sources of contamination: outgassing from the interior of the trap, and impurities in the helium buffer gas. Since the Paul trap chamber has a baseline vacuum of 4×10^{-10} mbar, it is unlikely that outgassing is the main source of the contamination. However, the helium gas is supplied with a grade of 5.7, meaning that the gas is 99.9997% helium. Applying the ideal gas law inside the volume of the Paul trap ($0.12\,\mathrm{L} = 1.2 \times 10^{-4}\,\mathrm{m}^3$) gives an approximation for the number of contaminant particles, where p_{cont} is the percent of contamination from the helium bottle:

$$N = \frac{PV}{k_b T} \Rightarrow N_{total} = \frac{(3.2 \times 10^{-7}\,\mathrm{bar})(1.2 \times 10^{-4}\,\mathrm{m}^3)}{k_b(293\,\mathrm{K})} = 9.54 \times 10^{14}\,\mathrm{atoms} \tag{32}$$

$$N_{cont} = N_{total} \times p_{cont} = 9.54 \times 10^{14}\,\mathrm{atoms} \times (1 - 0.999997) = 2.86 \times 10^{9}\,\mathrm{atoms} \tag{33}$$

Thus, despite the high purity He gas, there remains a large number of potential contaminant gas particles which can contribute to charge exchange. In order to remove the potential contamination from the helium gas, a liquid nitrogen trap could be employed in future applications to freeze out any other gases from the buffer gas line.

In the following Sections (5.4 and 5.5), all studies are performed in respect to the main ToF peak seen at 19 µs.

5.4 Buffer gas pressure

The buffer gas is a critical component of the Paul trap operation, as it is the primary agent for dissipating the energy of the ions. The room-temperature gas is leaked into the trapping volume, after which the ions will collide with the atoms, decreasing their overall energy.

There are two primary factors when choosing a gas to act as a coolant: the mass of the ions of interest, and the ionization energy of the gas. In order to minimize destabilizing effects from the buffer gas, the mass of the ions of interest should be much larger than the mass of the gas [55]. This is what leads to an overall decrease in energy, as it ensures that collisions are more likely to remove energy from the ions rather than increase energy while being confined in the Paul trap. The gas also needs a high ionization energy, otherwise there will be significant charge exchange of the coolant with the ions, which will be described later in this section. Based on these considerations, helium was selected as an appropriate buffer gas due to its low mass and high ionization energy.

The amount of buffer gas in the Paul trap is therefore an important factor in defining the bunch width and number of ions per bunch. Figure 22 shows these two quantities as a function of in-trap pressure on the left [3].

3. Measuring the pressure inside the Paul trap directly is not possible, so the pressure reported is estimated from simulations and the measured gas pressure in the vacuum chamber hosting the Paul trap. See [51]

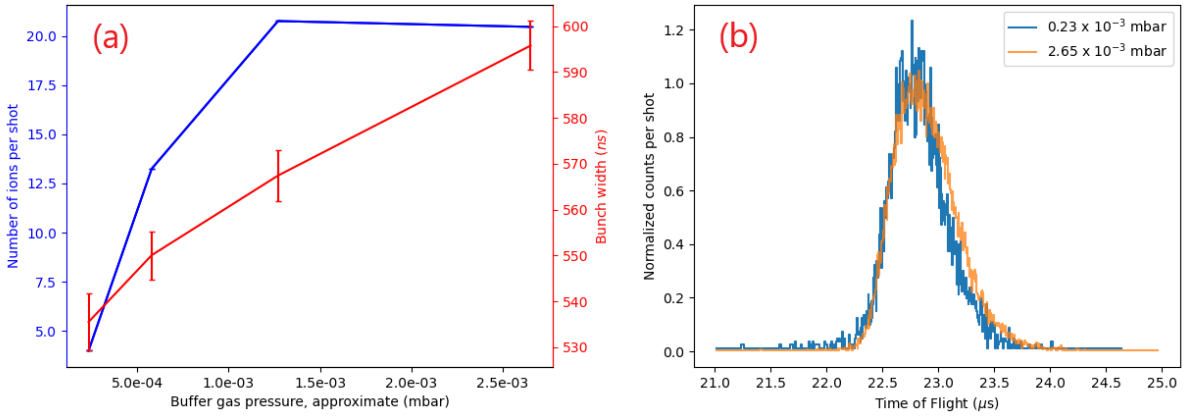

Figure 22 – (a) Number of ions per shot and bunch width expressed in FWHM as functions of in-trap pressure. (b) Two overlapping ToF spectra with the lowest and highest recorded pressures normalized in intensity. Experimental parameters: RF parameters = 200 V, 2 MHz, Paul trap floating = +265 V, loading time = 500 μs, cooling time = 30 ms, buffer gas pressure = variable, Endcap and endcone voltages during extraction = 100, -300 V in respect to its HV cage

Two features are immediately visible from the plot on the left. As the buffer gas pressure increases, so do the number of ions in the bunch, eventually reaching a saturation limit. As the pressure increases, incoming ions are more likely to collide often enough with the atoms to lose sufficient energy to become trapped; this explains why an increased pressure leads to more ions per bunch. Eventually, all incoming ions are captured and the number of ions per bunch can no longer increase, so increasing the buffer gas past this limit will not trap more ions.

There is also a clear increase in FWHM with increasing buffer gas pressure. This effect has two potential explanations: space charge issues with the increasing number of ions, or reheating during ion extraction and acceleration. During trapping and cooling, ions fall into the potential minimum of the Paul trap. Increasing the number of ions also increases the amount of charge in the trap well. The positive charges of the ions will repulse each other due to the Coulomb force if they try to occupy the same volume, which happens at the potential minimum. The increased Coulomb force causes the bunch to occupy a larger volume, which translates to a larger width of the extracted ion bunch. Below the saturation limit, a higher buffer gas pressure will result in more incoming ions being slowed down and trapped

by the DC potential, which could result in space charge effects being visible in the ion bunch structure.

The increase in bunch width could also be explained by reheating, an effect briefly mentioned in Section 5.1 to explain the tail visible on the ToF spectra in Figure 19. Reheating occurs during extraction when a cooled ion collides with the buffer gas in the re-acceleration path, e.g. in the region of the endcone, leading to a less Gaussian energy distribution. This alteration in the distribution is reflected in the ToF spectrum, as less energetic ions will arrive later at the magneTOF detector compared to the ions that did not undergo a collision with a He atom. This results in a tail on the ToF spectrum; the right panel of Figure 22 shows this effect, as the tail of the distribution measured with a higher buffer gas pressure extends past the right side of the distribution of the lower buffer gas pressure (whereas the left side of the data overlaps with each other for both pressure values).

Establishing reheating as the primary contributor to the increase in bunch temporal width is further supported by comparing the two lines in Figure 22 (a), in particular at higher pressure. Although the number of ions reaches a saturation point at $p \sim 1.5 \times 10^{-3}$ mbar, the ion bunch temporal width continues increasing when raising the buffer gas pressure. Since the number of ions per bunch remains constant in this region, an increase in bunch temporal width cannot be indicative of space charge effects, as they are dependent on additional ions per bunch.

Figure 22 (b) shows the normalized ToF spectra for the lowest and highest buffer gas pressures. While both spectra exhibit tails, the orange, higher pressure distribution extends significantly past the bounds of the blue distribution recorded a low Paul trap pressure. This results in an overall larger ion bunch width. Simulation studies at MIRACLS suggest that space charge effects do not typically appear for ion count rates ~ 20 ions/shot, and, if they do appear, would instead present themselves as deviations in the very end of the bunch tail with significant overlapping between the two main bunch structures. However, the observed data show a large deviation of the distribution starting immediately after the peak which is currently not fully understood.

Overall, the present data suggests that the observed increase in ion bunch width with larger buffer gas pressure is more likely due to reheating during the ion reacceleration, but

more work is needed to unambiguously confirm this conclusion.

5.5 Bunch extraction

The method of extraction is controlled via two electrodes of the Paul trap: the extraction endcap and extraction endcone. As described in Section 4.4.2, the endcaps are primarily responsible for opening and closing the Paul trap, while the endcones are used to help focus the beam. This section investigates the effects of both parameters on the ion bunch.

Figure 23 shows the (a) counts per shot and (b) temporal ion bunch width as functions of the extraction potentials. The most significant feature of the plots is the effect of the endcap on the temporal ion bunch width; a more negative endcap potential leads to a smaller FWHM, whereas the endcone has a negligible effect. A more negative voltage applied to the endcap creates a sharper potential curve inside the trap, essentially "kicking" the bunch out of the trap. A more shallow potential gradient during extraction leads to a smaller energy spread in the bunch, but also to a wider ion-bunch width. The endcone does not have this effect on the bunch width as the endcap shields the trap interior from the voltage applied on the endcone; this is reflected in the measured data, where the lines are effectively horizontal in Figure 23 (b) when varying the endcone voltage.

However, the endcone and endcap voltages both affect the number of ions per shot, as seen in Figure 23 (a). The highest ion numbers per measurement cycle is obtained for low (absolute) potentials applied to the endcap and endcone. This observation is not fully understood but could be the result of focusing effects and the resulting trajectory down the beamline until the magneTOF detector. If the endcap voltage is sufficiently lowered and the endcone kept much less negative, this configuration paired with the potential minimum in the Paul trap generated by the DC electrodes could act as an einzel lens. This could cause an unintended focus along the ion beam path between the extraction from the trap such that a fraction of the ions do not reach the magneTOF detector, although the ions were successfully extracted from the Paul trap. More work is thus needed to understand the observed dependence of the ion intensity on the potentials applied to the endcone and endcap.

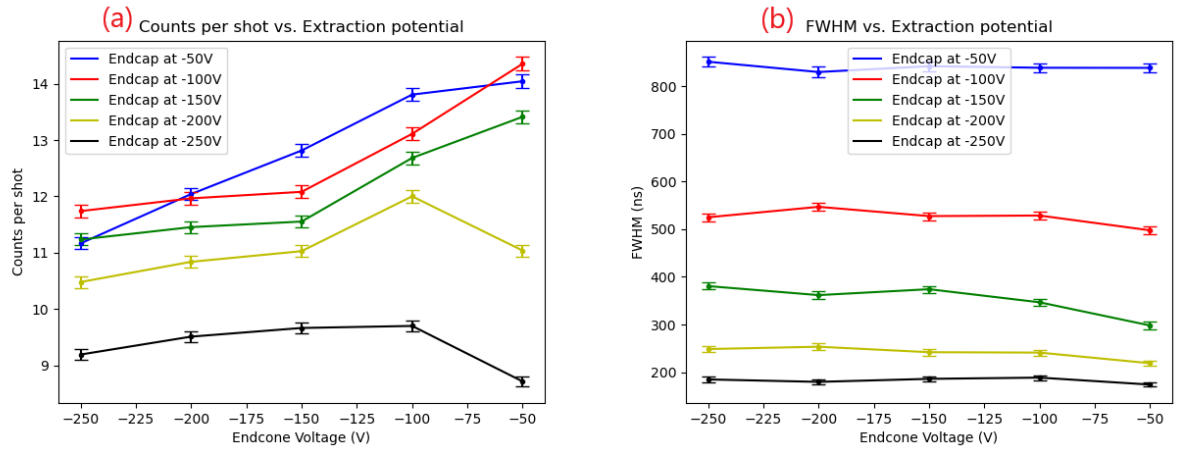

Figure 23 – (a) Number of ions per shot as a function of extraction potentials. (b) Bunch width as a function of extraction potentials. Experimental parameters: RF parameters = 200 V, 2 MHz, Paul trap floating = +265 V, loading time = 500 μs, buffer gas pressure = 3.2 $\times 10^{-4}$ mbar, Endcap and endcone voltages = variable

Lastly, Figure 24 shows the ToF centroid of the ion bunch as a function the extraction potentials. As expected, more negative potentials lead to an earlier arrival of the bunch at the magneTOF detector. Since the bunch is extracted from the trap in less time, it arrives faster at the detector. The effect of the endcap on the temporal location of the bunch center is stronger than the effect of the endcone, which is also expected since the very initial acceleration, still inside the trap region, is primarily due to the endcap as explained in the two paragraphs above.

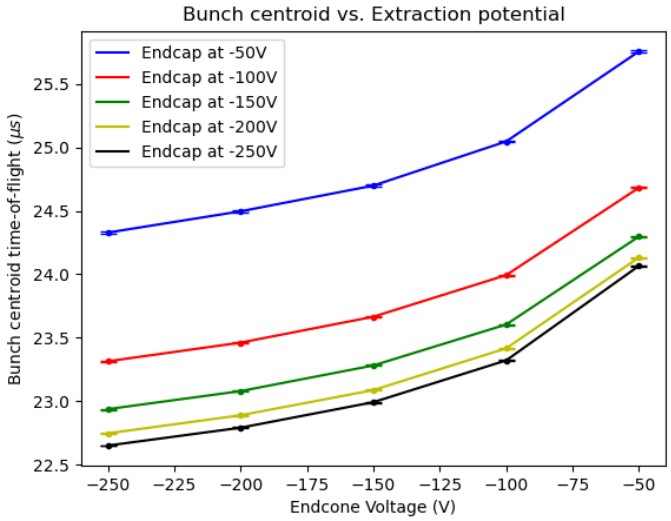

Figure 24 – ToF centroid as a function of extraction potentials. The same experimental parameters as the previous two plots were used.

5.6 Best achieved Paul trap performance for MIRACLS operation

The purpose of this Paul trap in the MIRACLS setup is to provide cooled bunches to the 30 keV MR-ToF instrument. As stated in Section 4.4.1, the 30 keV CLS measurement in the MR-ToF apparatus requires a bunch energy spread of less than 1 eV and a temporal width of less than 700 ns [36, 49]. Simulations of the beamline with a beam transport energy of 2 keV and 50 keV show no change in the temporal bunch width nor the energy spread requirements of the experiment [56].

These same simulations show that it is important to consider the energy spread of the bunch when selecting parameters. Due to the conservation of emittance, a low temporal width obliges a large energy spread, and vice versa. When using the in-trap lift technique to trap the bunch in the MR-ToF device, bunches with large temporal widths can be chopped and ions lost. Conversely, large energy spreads significantly increase Doppler broadening during CLS measurements, and are detrimental to the CLS measurement resolution. Comparisons between the energy spreads of the simulations and this first study remain challenging, given the need for specific devices to measure experimentally the energy spread. Once the MR-ToF apparatus is commissioned, the energy spread can be estimated by measuring the signal during the CLS measurement and comparing it to the results of the simulations.

However, it remains clear that the results of this study exceed the requirements necessary for a more energetic beam. In the present study, the smallest temporal width achieved was 123 ns for the fitted FWHM, with an average of 3.31 counts per shot. This spectrum is presented in Figure 25. It is achieved with the parameters presented in Table 2. This time spread is almost a factor of 4 smaller than the requirements for optimal MR-ToF operation, but can be increased in the aim of decreasing the energy spread of the bunch.

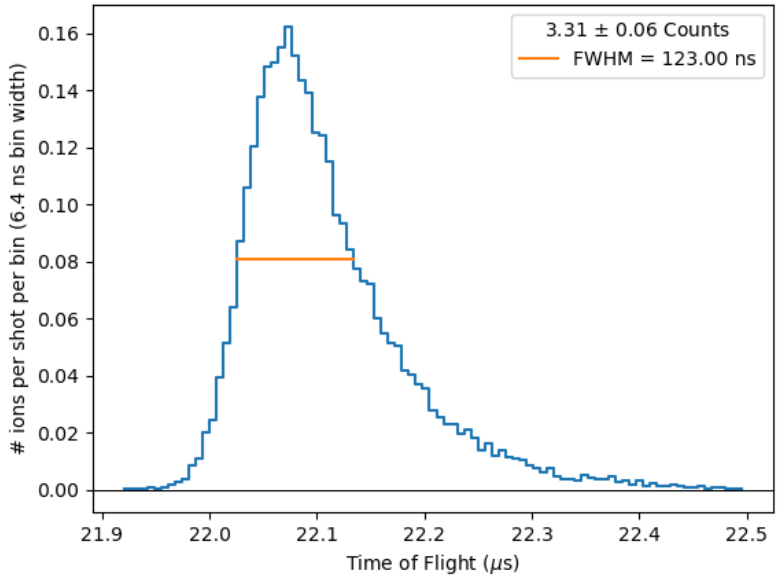

Figure 25 – ToF spectrum for the best recorded bunch temporal width

Parameter	**Value**
RF Amplitude	200 V
RF Frequency	2 MHz
Paul trap floating	+260 V
Loading time	500 μs
Cooling time	85 ms
Buffer gas pressure	6×10^{-5} mbar
Endcap potential	-300 V
Endcone potential	-300 V

Table 2 – Parameters to achieve best result for temporal width of the ion bunch

Decreasing the ion bunch temporal width further is also possible without installing additional devices by utilizing the results from this study. For example, the dependence of the bunch centroid on the extraction configuration, presented in Figure 24, is useful in calibrating the extraction timings with the RF potential phase. The RF field changes the longitudinal DC potential as well, resulting in individual ion micromotion along the axis of the Paul trap. This can have an unintended effect on the bunch and either add or remove energy, depending on the moment the bunch is extracted. Although this effect cannot be removed, the systematic uncertainty in position that arises from it can be mitigated by consistently extracting the bunch at the same point in the RF cycle. This can be done in future work by synchronizing the moment of the ion extraction with the phase of the RF potential.

6 Conclusion

In this thesis, the installation, commissioning, and first characterization of the Paul trap in the Multi-Ion Reflection Apparatus for Collinear Laser Spectroscopy (MIRACLS) was discussed. An overview of the Paul trap experimental setup was provided, as well as extensive details on the MIRACLS experiment's goals and motivations.

Ion traps have revolutionized numerous fields of physics for their multitude of uses, and have proved themselves as critical pieces of infrastructure for nuclear physics experiments. The novel MIRACLS technique improves the sensitivity of experiments on short lived radionuclides by performing collinear laser spectroscopy inside a Multiple-Reflection Time-of-Flight (MR-ToF) device; by trapping and revolving the ion bunches, MIRACLS is able to extend the interaction time of the ion beam with an overlapping laser while maintaining the high resolution of conventional collinear laser spectroscopy (CLS).

In order to couple the continuous, fast-ion beam delivered by ISOLDE with effective MR-ToF operation, a Paul trap was designed and constructed to cool and bunch the initial radioactive beam. The Paul trap serves to provide ion bunches with beam energies of ≈ 50 keV and low beam emittance of temporal widths less than 700 ns as well as an energy spread lower than 1 eV as required for MR-ToF operation at MIRACLS. This allows for minimal ion losses in the MR-ToF device as well as minimal Doppler broadening while conserving a high beam energy, which results in a high spectroscopic resolution.

The first science case for MIRACLS is the study of neutron-deficient and neutron-rich magnesium isotopes. As such, the characterization of the new Paul was conducted using an offline electron impact ionization ion source providing stable beam of Mg ions. This ion source is located in a branch downstream from the Paul trap. The continuous ion beam from the source was reversely directed into the Paul trap, after which the ions were cooled and bunched. The bunched ions are then extracted from the same direction as they were injected, and directed to a magneTOF detector in order to measure the time-of-flight spectrum of the ion bunch.

Using this setup, the commissioning and characterization of the Paul trap was successful, and the results discussed in this work. The Paul trap is able to trap ions from the offline

source, cool the ions, and extract them as ion bunches. Expected characteristics of cooled bunches are observed, and various operating parameters can be controlled in order to maximize the quality of the bunches.

The Paul trap RF stability has been characterized and overall matches results from simulations of this system. The operating parameters for magnesium studies were selected to be 200 V200 for the RF amplitude and 1.6 MHz for the RF frequency. The optimal cooling time is $\approx 10-30$ ms; larger cooling times were observed to cause charge exchange, an undesirable effect where ions of interest are lost to contaminants. Buffer gas pressure is also an important parameter of Paul trap operation, as too high a pressure can lead to reheating effects on the ion bunch during extraction or space charge up during cooling, both of which will increase the temporal bunch width. The extraction parameters are the last important parameters that directly influence the bunch width. The endcap voltage was determined to have the largest effect on the temporal spread and number of ions, but a combination of both endcap and endcone potentials is necessary to optimize the trap performance. It was also concluded that the Paul trap meets the operating requirements for the MIRACLS MR-ToF device.

The next steps of MIRACLS are to complete the assembly of the remaining MIRACLS components and commission the MR-ToF instrument in preparation for its first online study with radioactive magnesium beam from ISOLDE. Although the MIRACLS collaboration has already been successful in performing CLS inside a low energy MR-ToF device, this will mark the first time that an MR-ToF device operates at an energy of 30 keV, and mark the first time CLS is performed in an MR-ToF on a Radioactive Ion Beam (RIB) beamline. Future studies of cadmium isotopes are planned following the successful investigation of magnesium. The critical components of the MIRACLS beamline, including the Paul trap and MR-ToF device, will ultimately be installed as a permanent fixture as the ISOLDE MR-ToF mass-separator. The first experiment benefiting from the ISOLDE MR-ToF instrument will be the antiProton Unstable Matter Annihilation experiment (PUMA).

References

[1] W. Paul and H. Steinwedel, "A new mass spectrometer without a magnetic field," *Zeitschrift fuer Naturforschung (West Germany) Divided into Z. Nautrforsch., A, and Z. Naturforsch., B: Anorg. Chem., Org. Chem., Biochem., Biophys.,*, vol. a8, 7 1953. 1

[2] R. S. Van Dyck, P. B. Schwinberg, and H. G. Dehmelt, "Electron magnetic moment from geonium spectra: Early experiments and background concepts," *Phys. Rev. D*, vol. 34, pp. 722–736, Aug 1986. 1

[3] D. Hanneke, S. Fogwell, and G. Gabrielse, "New measurement of the electron magnetic moment and the fine structure constant," *Phys. Rev. Lett.*, vol. 100, p. 120801, Mar 2008. 1

[4] X. Fan, T. G. Myers, B. A. D. Sukra, and G. Gabrielse, "Measurement of the electron magnetic moment," 2022. 1

[5] G. Graff, H. Kalinowsky, and J. Traut, "A Direct Determination of the Proton Electron Mass Ratio," *Z. Phys. A*, vol. 297, pp. 35–39, 1980. 1

[6] R. S. Van Dyck, P. B. Schwinberg, and H. G. Dehmelt, "New high-precision comparison of electron and positron g factors," *Phys. Rev. Lett.*, vol. 59, pp. 26–29, Jul 1987. 1

[7] "The nobel prize in physics 1989," Oct 1989. 1

[8] N. Foundation, *Physics, 1963-1970*. Nobel Lectures in Physics, World Scientific, 1998. 3

[9] D. J. Dean and M. Hjorth-Jensen, "Pairing in nuclear systems: from neutron stars to finite nuclei," *Rev. Mod. Phys.*, vol. 75, pp. 607–656, Apr 2003. 3

[10] M. G. Mayer, "Nuclear configurations in the spin-orbit coupling model. i. empirical evidence," *Phys. Rev.*, vol. 78, pp. 16–21, Apr 1950. 3

[11] O. Haxel, J. H. D. Jensen, and H. E. Suess, "On the "magic numbers" in nuclear structure," *Phys. Rev.*, vol. 75, pp. 1766–1766, Jun 1949. 3

[12] Y. Yu and A. Bulgac, "Appendix to: Energy density functional approach to superfluid nuclei, nucl-th/0210047," 03 2003. 4

[13] Á. Koszorús, X. F. Yang, W. G. Jiang, S. J. Novario, S. W. Bai, J. Billowes, C. L. Binnersley, M. L. Bissell, T. E. Cocolios, B. S. Cooper, R. P. de Groote, A. Ekström, K. T. Flanagan, C. Forssén, S. Franchoo, R. F. G. Ruiz, F. P. Gustafsson, G. Hagen, G. R. Jansen, A. Kanellakopoulos, M. Kortelainen, W. Nazarewicz, G. Neyens, T. Papenbrock, P.-G. Reinhard, C. M. Ricketts, B. K. Sahoo, A. R. Vernon, and S. G. Wilkins, "Charge radii of exotic potassium isotopes challenge nuclear theory and the magic character of n = 32," *Nature Physics*, vol. 17, pp. 439–443, jan 2021. 5

[14] C. Bertulani, "Nuclear physics in a nutshell," *Nuclear Physics in a Nutshell, by Carlos A. Bertulani. ISBN 978-0-691-12505-3. Published by Princeton University Press, Princeton, NJ USA, 2007.*, 01 2007. 7

[15] S. B. Welles, "Electric quadrupole moments of light and heavy nuclei," *Phys. Rev.*, vol. 62, pp. 197–203, Sep 1942. 7

[16] G. Neyens, "Nuclear magnetic and quadrupole moments for nuclear structure research on exotic nuclei," *Reports on Progress in Physics*, vol. 66, p. 633, mar 2003. 7

[17] T. Aumann *et al.*, "PUMA, antiProton unstable matter annihilation," *Eur. Phys. J. A*, vol. 58, no. 5, p. 88, 2022. 8

[18] R. Hofstadter, "Nuclear and nucleon scattering of high-energy electrons," *Annual Review of Nuclear Science*, vol. 7, no. 1, pp. 231–316, 1957. 8

[19] N. Bohr, "I. on the constitution of atoms and molecules," *The London, Edinburgh, and Dublin Philosophical Magazine and Journal of Science*, vol. 26, no. 151, pp. 1–25, 1913. 9

[20] J. Boyd, "New schrödinger wave mathematics changes experiments from saying there is, to denying there is quantum weirdness : It changes how the quantum world works," *Journal of Advances in Mathematics*, vol. 18, p. 72–117, Feb. 2020. 10

[21] C. Foot, *Atomic Physics*. Oxford Master Series in Physics, OUP Oxford, 2005. 11

[22] B. Cheal and K. T. Flanagan, "Progress in laser spectroscopy at radioactive ion beam facilities," *Journal of Physics G: Nuclear and Particle Physics*, vol. 37, p. 113101, sep 2010. 12

[23] J. Persson, "Table of hyperfine anomaly in atomic systems," *Atomic Data and Nuclear Data Tables*, vol. 99, pp. 62–68, jan 2013. 12

[24] R. Neugart, J. Billowes, M. L. Bissell, K. Blaum, B. Cheal, K. T. Flanagan, G. Neyens, W. Nörtershäuser, and D. T. Yordanov, "Collinear laser spectroscopy at isolde: new methods and highlights," *Journal of Physics G: Nuclear and Particle Physics*, vol. 44, p. 064002, apr 2017. 13

[25] K. Blaum, J. Dilling, and W. Nörtershäuser, "Precision atomic physics techniques for nuclear physics with radioactive beams," *Physica Scripta*, vol. T152, p. 014017, jan 2013. 13

[26] S. Kaufman, "High-resolution laser spectroscopy in fast beams," *Optics Communications*, vol. 17, no. 3, pp. 309–312, 1976. 13

[27] R. Catherall, W. Andreazza, M. Breitenfeldt, A. Dorsival, G. J. Focker, T. P. Gharsa, G. T. J, J.-L. Grenard, F. Locci, P. Martins, S. Marzari, J. Schipper, A. Shornikov, and T. Stora, "The isolde facility," *Journal of Physics G: Nuclear and Particle Physics*, vol. 44, p. 094002, aug 2017. 14, 15

[28] F. M. Maier, P. Fischer, H. Heylen, V. Lagaki, S. Lechner, P. Plattner, S. Sels, F. Wienholtz, W. Nörtershäuser, L. Schweikhard, and S. Malbrunot-Ettenauer, "Simulations of a proof-of-principle experiment for collinear laser spectroscopy within a multi-reflection time-of-flight device," *Hyperfine Interactions*, vol. 240, pp. 1–13, May 2019. 14, 17, 30

[29] V. Lagaki, H. Heylen, I. Belosevic, P. Fischer, C. Kanitz, S. Lechner, F. Maier, W. Nörtershäuser, P. Plattner, M. Rosenbusch, S. Sels, L. Schweikhard, M. Vilen, F. Wienholtz, R. Wolf, and S. Malbrunot-Ettenauer, "An accuracy benchmark of the miracls apparatus: Conventional, single-passage collinear laser spectroscopy inside a mr-tof device," *Nuclear Instruments and Methods in Physics Research Section A: Accelerators, Spectrometers, Detectors and Associated Equipment*, vol. 1014, p. 165663, 2021. 14, 17

[30] S. Sels, P. Fischer, H. Heylen, V. Lagaki, S. Lechner, F. Maier, P. Plattner, M. Rosenbusch, F. Wienholtz, R. Wolf, W. Nörtershäuser, L. Schweikhard, and S. Malbrunot-Ettenauer, "First steps in the development of the multi ion reflection apparatus for

collinear laser spectroscopy," *Nuclear Instruments and Methods in Physics Research Section B: Beam Interactions with Materials and Atoms*, vol. 463, pp. 310–314, 2020. 14, 17

[31] T. Dickel, W. Plaß, A. Becker, U. Czok, H. Geissel, E. Haettner, C. Jesch, W. Kinsel, M. Petrick, C. Scheidenberger, A. Simon, and M. Yavor, "A high-performance multiple-reflection time-of-flight mass spectrometer and isobar separator for the research with exotic nuclei," *Nuclear Instruments and Methods in Physics Research Section A: Accelerators, Spectrometers, Detectors and Associated Equipment*, vol. 777, pp. 172–188, 2015. 16

[32] P. Schury, M. Wada, Y. Ito, S. Naimi, T. Sonoda, H. Mita, A. Takamine, K. Okada, H. Wollnik, S. Chon, H. Haba, D. Kaji, H. Koura, H. Miyatake, K. Morimoto, K. Morita, and A. Ozawa, "A multi-reflection time-of-flight mass spectrograph for short-lived and super-heavy nuclei," *Nuclear Instruments and Methods in Physics Research Section B: Beam Interactions with Materials and Atoms*, vol. 317, pp. 537–543, 2013. XVIth International Conference on ElectroMagnetic Isotope Separators and Techniques Related to their Applications, December 2–7, 2012 at Matsue, Japan. 16

[33] F. Wienholtz *et al.*, "Masses of exotic calcium isotopes pin down nuclear forces," *Nature*, vol. 498, no. 7454, pp. 346–349, 2013. 16

[34] F. Wienholtz, D. Atanasov, S. Kreim, V. Manea, M. Rosenbusch, L. Schweikhard, A. Welker, and R. N. Wolf, "Towards ultrahigh-resolution multi-reflection time-of-flight mass spectrometry at isoltrap," *Physica Scripta*, vol. 2015, p. 014068, nov 2015. 16

[35] P. Fischer and L. Schweikhard, "Multiple active voltage stabilizations for multi-reflection time-of-flight mass spectrometry," *Review of Scientific Instruments*, vol. 92, no. 6, p. 063203, 2021. 16

[36] F. M. Maier, "Laser spectroscopy of short-lived- radionuclides in an ion trap: Miracls' proof-of-principle experiment and the simulation of the future 30-kev mr-tof device," Master's thesis, JOHANNES KEPLER UNIVERSITY LINZ, 2019. 16, 29, 50

[37] M. Vilen, S. Malbrunot-Ettenauer, P. Fischer, H. Heylen, V. Lagaki, S. Lechner, F. M. Maier, W. Nortershauser, P. Plattner, S. Sels, and et al., "Miracls at isolde: The charge

radii of exotic magnesium isotopes," May 2020. 18

[38] J. Ballof *ISOLDE Yield Database*, November 2021. 18

[39] R. N. Wolf, G. Marx, M. Rosenbusch, and L. Schweikhard, "Static-mirror ion capture and time focusing for electrostatic ion-beam traps and multi-reflection time-of-flight mass analyzers by use of an in-trap potential lift," *International Journal of Mass Spectrometry*, vol. 313, pp. 8–14, 2012. 19

[40] D. Stresau, K. Hunter, W. Sheils, P. Raffin, and Y. Benari, "A new class of robust sub-nanosecond tof detectors with high dynamic range," tech. rep., ETP Electron Multipliers, Ermington, Australia. 19, 27, 28

[41] S. Earnshaw, "On the Nature of the Molecular Forces which Regulate the Constitution of the Luminiferous Ether," *Transactions of the Cambridge Philosophical Society*, vol. 7, p. 97, Jan. 1848. 21

[42] W. Paul, "Electromagnetic traps for charged and neutral particles," *Rev. Mod. Phys.*, vol. 62, pp. 531–540, Jul 1990. 21, 22, 23

[43] L. Ruby, "Applications of the mathieu equation," *American Journal of Physics*, vol. 64, no. 1, pp. 39–44, 1996. 23

[44] J. Heinrich, *A Be+ Ion Trap for H2+ Spectroscopy*. PhD thesis, Sorbonne Université, 04 2018. 23, 24

[45] M. Smith, *A square-wave-driven radiofrequency quadrupole cooler and buncher for TITAN*. PhD thesis, University of British Columbia, 2005. 24

[46] R. B. Moore, A. M. G. Dezfuli, P. Varfalvy, H. Zhao, and T. ISOLDE-Collaboration, "Production, transfer and injection of charged particles in traps and storage rings," *Physica Scripta*, vol. 1995, p. 93, jan 1995. 24, 25

[47] D. A. Edwards and J. J. Syphers, "An introduction to the physics of high energy accelerators," 1 1993. 25

[48] T. Murböck, S. Schmidt, Z. Andelkovic, G. Birkl, W. Nörtershäuser, and M. Vogel, "A compact source for bunches of singly charged atomic ions," *Review of Scientific Instruments*, vol. 87, p. 043302, 04 2016. 29

[49] F. Maier, M. Vilen, I. Belosevic, F. Buchinger, C. Kanitz, S. Lechner, E. Leistenschneider, W. Nörtershäuser, P. Plattner, L. Schweikhard, S. Sels, F. Wienholtz, and S. Malbrunot-Ettenauer, "Simulation studies of a 30-kev mr-tof device for highly sensitive collinear laser spectroscopy," *Accepted in Nuclear Inst. and Methods in Physics Research, A*, 2022. 29, 50

[50] S. Lechner, *Laser Spectroscopy of Antimony Isotopes and the Design of a Cryogenic Paul trap*. PhD thesis, Technische Universitaet Wien, 2021. 31

[51] C. Kanitz, "Construction and characterization of a paul trap for laser spectroscopy of exotic radionuclides in an mr-tof device," Master's thesis, Friedrich-Alexander-Universität Erlangen-Nürnberg, 2021. 31, 41, 45

[52] E. J. Catanzaro, T. J. Murphy, E. L. Garner, and W. R. Shields, "Absolute isotopic abundance ratios and atomic weight of magnesium.," *Journal of research of the National Bureau of Standards. Section A, Physics and chemistry*, vol. 70A 6, pp. 453–458, 1966. 40

[53] A. Nieminen, J. Huikari, A. Jokinen, J. Äystö, P. Campbell, and E. Cochrane, "Beam cooler for low-energy radioactive ions," *Nuclear Instruments and Methods in Physics Research Section A: Accelerators, Spectrometers, Detectors and Associated Equipment*, vol. 469, no. 2, pp. 244–253, 2001. 40

[54] F. Herfurth, J. Dilling, A. Kellerbauer, G. Bollen, S. Henry, H.-J. Kluge, E. Lamour, D. Lunney, R. Moore, C. Scheidenberger, S. Schwarz, G. Sikler, and J. Szerypo, "A linear radiofrequency ion trap for accumulation, bunching, and emittance improvement of radioactive ion beams," *Nuclear Instruments and Methods in Physics Research Section A: Accelerators, Spectrometers, Detectors and Associated Equipment*, vol. 469, pp. 254–275, aug 2001. 43

[55] M. Green, J. Wodin, R. DeVoe, P. Fierlinger, B. Flatt, G. Gratta, F. LePort, M. Montero Díez, R. Neilson, K. O'Sullivan, A. Pocar, S. Waldman, D. S. Leonard, A. Piepke, C. Hargrove, D. Sinclair, V. Strickland, W. Fairbank, K. Hall, B. Mong, M. Moe, J. Farine, D. Hallman, C. Virtue, E. Baussan, Y. Martin, D. Schenker, J.-L. Vuilleumier, J.-M. Vuilleumier, P. Weber, M. Breidenbach, R. Conley, C. Hall, J. Hodgson,

D. Mackay, A. Odian, C. Y. Prescott, P. C. Rowson, K. Skarpaas, and K. Wamba, "Observation of single collisionally cooled trapped ions in a buffer gas," *Phys. Rev. A*, vol. 76, p. 023404, Aug 2007. 45

[56] F. Maier. Personal communication. 50